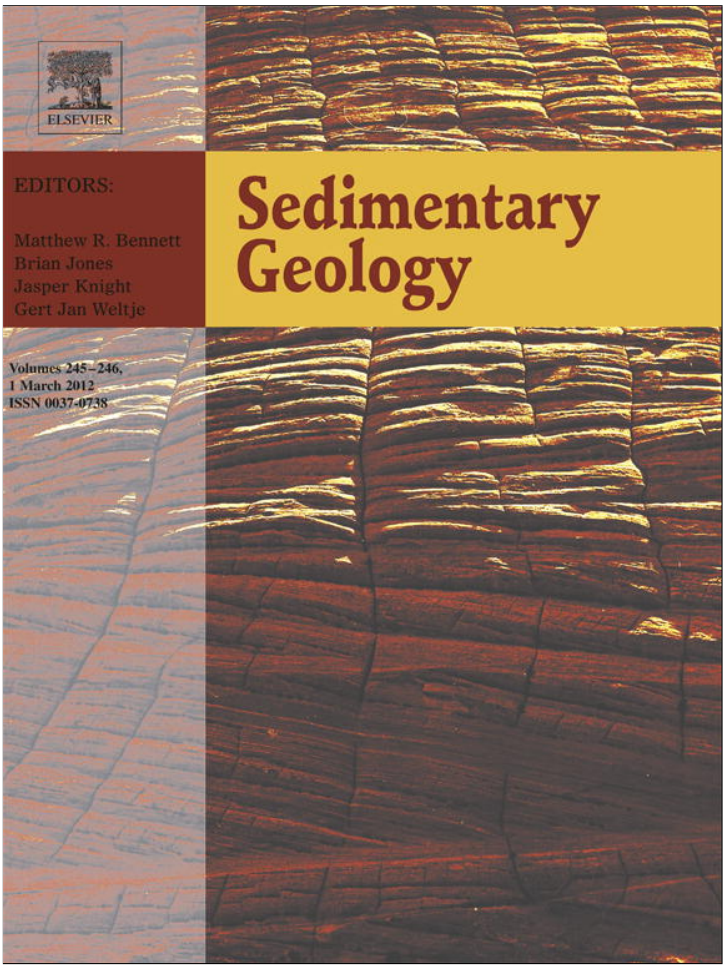

Sedimentary Geology 245–246 (2012) 29–47

Contents lists available at SciVerse ScienceDirect

Sedimentary Geology

journal homepage: www.elsevier.com/locate/sedgeo

Dynamic controls on accretion and lithification of modern gypsum-dominated thrombolites, Los Roques, Venezuela

Daniel A. Petrash [a,*], Murray K. Gingras [a], Stefan V. Lalonde [b], François Orange [a], Ernesto Pecoits [a], Kurt O. Konhauser [a]

[a] Department of Earth and Atmospheric, University of Alberta, Edmonton, Alberta, Canada T6G 2E3
[b] Laboratoire Domaines Océaniques, Institut Universitaire Européen de la Mer, Université de Bretagne Occidentale, Place Nicholas Copernic, Technopôle Brest-Iroise, 29280 Plouzané, France

ARTICLE INFO

Article history:
Received 29 May 2011
Received in revised form 7 December 2011
Accepted 7 December 2011
Available online 16 December 2011

Editor: B. Jones

Keywords:
Microbial mats
Microbialites
Anoxygenic photosynthesis
Exopolymers
Trace metals

ABSTRACT

Meter-sized thrombolites coated by well developed zonally differentiated microbial mats have been found growing in the shallow waters (depth < 1 m) of a restricted hypersaline lagoon on the Archipelago Los Roques in Venezuela. By contrast, within the deeper parts of the studied lagoon, sedimentation is characterized by several decimeters of organic-rich material containing gypsum granules lacking carbonate cementation. The lithification of the thrombolites is thought to have proceeded as follows. First, extracellular polymeric substances (EPS) comprising the microbial mat concentrate Ca^{2+} and other metal cations by adsorption from the hypersaline waters. Second, some of these bound metals then serve as nucleation sites for primary calcium carbonate ($CaCO_3$) precipitation. Third, while carbonate phases are forming in some zones of the mat, in others zones they are being re-dissolved due to the acidity generated through the metabolism of sulfide-oxidizing bacteria, Fourth, as the dissolved sulfide is oxidized into sulfate, the pore-water become saturated with respect to gypsum ($CaSO_4 \cdot 2H_2O$). Fifth, as primary gypsum precipitates within the structures, endolithic sulfate-reducing bacteria metabolize the sulfate moiety in the mineral phase, while simultaneously oxidizing the EPS trapped during accretion. Sixth, as microbial EPS degradation proceeds, the anaerobic oxidation of specific protein fractions of the EPS matrix leads to increased alkalinity, the partial dissolution of gypsum, supersaturation with respect to calcium carbonate, and ultimately pseudomorphic aragonite replacement; this differs from secondary calcite cements in being enriched in ^{12}C, and depleted in minor and trace metals initially associated with the EPS. The biogeochemical processes occurring in this thrombolite-constructing lagoon represent a novel field site for studying the chemical and isotopic processes characterizing early diagenetic gypsum and the role microbes play in its precipitation, dissolution and calcification. In this regard, insights gained from this modern field site will help to better understand mechanisms by which some Precambrian microbialites were lithified.

1. Introduction

Microbialites are accretionary organosedimentary structures that form as a result of a benthic microbial community trapping and binding detrital sediment and/or forming the locus of mineral precipitation (Burne and Moore, 1987). Accordingly, stromatolites (Kalkowsky, 1908) and thrombolites (Aitken, 1967) are distinct types of microbialites characterized, respectively by laminated and mesoclotted internal fabrics (Kennard and James, 1986; Riding, 2011). Both stromatolites and thrombolites typically develop in shallow subaqueous settings, such as intertidal flats and hypersaline lagoons (Jørgensen et al., 1983; Des Marais, 2003), that are characterized by higher rates of organic matter production relative to grazing (Stal, 2000). During diagenesis, the organic matter serves as an electron donor to various microbial metabolisms, including sulfate reduction, that leads to (1) complex elemental cycling within the structures (Des Marais, 2003), (2) the enhancement of pore-water alkalinity (Slaughter and Hill, 1991), and (3) subsequent cementation by calcium carbonate (Visscher et al., 1998; Riding, 2011).

Despite being less common, gypsum has also been shown to play a role in microbialite accretion (e.g., Kobluk and Crawford, 1990; Vogel et al., 2010). Morphologically, fossil gypsum microbialites may occur as domes, columns or planar structures (Rouchy and Monty, 2000). Texturally, they are more commonly distinguished by their dominant internal thrombolitic fabric (Riding, 2000), which may locally interfinger with crudely laminar crusts to form thrombolitic stromatolites (Riding, 2011). The sulfate mineral is a seemingly minor, yet important component of the stromatolitic record (Rouchy and Monty, 2000; Pope et al., 2000; Riding, 2008), however, gypsum, as primary mineralogy, could be replaced early during diagenesis by carbonates (Vogel et al., 2010, and references therein). Hence, a more complete

* Corresponding author.
E-mail address: petrash@ualberta.ca (D.A. Petrash).

0037-0738/$ – see front matter © 2011 Elsevier B.V. All rights reserved.
doi:10.1016/j.sedgeo.2011.12.006

understanding of the mechanisms by which modern subaqueous gypsum-dominated thrombolites form today would be useful to understand their ancient diagenetically modified analogs; thereby the problem of the significance of dubious pseudomorphic features in the highly fragmented stromatolitic record could be addressed (see Riding, 2008, p. 77–78, for details).

The bacterial role in gypsum precipitation, as well as the effects that early gypsum precipitation may have in microbialite fabric development has yet to be fully explored, mostly because gypsum is rarely found in modern microbialites (Kobluk and Crawford, 1990; Rouchy and Monty, 2000). By using transmitted and reflected light, scanning electron microscopy (SEM), electron probe microanalysis (EPMA) and laser ablation-inductively coupled plasma mass spectrometry (LA-ICPMS), we describe here the biogeochemical and mineralogical processes occurring in an alkaline and hypersaline lagoon in the Archipelago Los Roques, Venezuela. In the shallower areas (to a depth of <1 m) complex photosynthetic microbial mats are associated with thrombolites. The mineralogy and texture of the decimeter- to meter-scale thrombolites from Los Roques differ from most modern occurrences because of the abundance of gypsum, which is being pseudomorphically replaced by aragonite; while the lithification of the structures is mostly due to micritization of aragonite pseudomorphs after gypsum.

The relationships between internal microfabrics, primary and secondary mineralogies, and the distribution of biochemical signatures have not been systematically studied in modern thrombolites. Specifically, we were interested in documenting: (1) the affinity of extracellular polysaccharide (EPS)-rich organic matrices for certain dissolved metals which may serve as "biological proxies" (Fazio et al., 1982; Decho, 1990; Decho et al., 2005; Perry et al., 2005; Braissant et al., 2007; Ortega-Morales et al., 2007; Flemming and Wingender, 2010); and (2) if the degradation of EPS trapped during accretion produces complex physicochemical conditions and influences cation fluxes and internal diffusion pathways towards active sites of reactive carbonate precipitation (e.g., Kamber et al., 2004; Braissant et al., 2009; Decho, 2010). Importantly, if unique trace metal trends are preserved in these modern thrombolites, it might then be possible to identify whether biological processes similarly led to the accretion of ancient thrombolites, and for that matter, stromatolites exhibiting heterogeneous internal fabrics.

2. Geological and environmental settings

The Archipelago comprising Los Roques National Park is located in the southern Caribbean Sea, approximately 150 km offshore of the Venezuelan mainland. The archipelago has 42 low-laying islands and a large number of sand banks distributed in an isolated, oval-shaped rimmed shelf (Fig. 1), approximately 1250 km^2 in extent. The inner shelf consists of a composite lagoon which has maximum and average water depths of 50 m and 5 m, respectively (Amend, 1992). The composite lagoon is partially enclosed by coral reefs, which are better developed along the eastern and southern margins of the archipelago (Fig. 1). The reef grades to sand banks that form supratidal islands which shelter the shelf from open ocean circulation and are frequently colonized by mangroves that partially confine the shallow seawaters by increasing sedimentation rates. In many of the low-laying emerged islands there are perennial hypersaline lagoons and/or ephemeral lagoons, both accompanied by supratidal sabkha deposits.

Climate in Los Roques is warm and humid with average air temperatures and daily humidity of 28 °C and 80%, respectively. Rainfall is scarce and rarely exceeds 270 mm yr^{-1}, the bulk of which falls during October through to January. Evaporation rates are up to 225 mm yr^{-1} (as estimated by Sonnenfeld et al., 1977), thus, evaporation exceeds precipitation most of the year and salinities in the restricted lagoons may reach values of up to 175‰.

The studied thrombolites were observed at Laguna Pirata, which is an anchialine lagoon restricted by a permeable Quaternary beach rock and a modern sandbank; thereby the evaporatively concentrated water is constantly fed by seepage seawater reflux (i.e. Babel, 2007). The lagoon has maximum and average depths of 1.6 and 0.5 m, respectively. The water body is density stratified and its hypolimnion consists of poorly oxygenated to sulfidic brine (Fig. 2). The average temperature of the shallow margins of the lagoon is 34 °C.

Sedimentation at the lagoon margins consists of whitish, finely crystalline crusts formed by evaporation. These crusts, which can be up to 3 cm thick, are polymineralic and contain halite, gypsum and aragonite, thus when dry they are easily erodible by ablation or can be partially dissolved by sporadic showers. Subaqueously, lithified domal-shaped thrombolites, with sizes ranging from less than 10 cm in diameter to larger coalesced structures up to 4 m large, develop along the shallow margins in a zone where water depths range from tens of centimeters down to about 1 m (Fig. 3A, B). The narrow actively-growing thrombolite zone is subparallel to the shore, where most of the subaqueous sedimentary substrate has been colonized by complex microbial mats up to 2 cm thick (Figs. 3C-F, 5). The actively growing thrombolite zone laterally gives way basinwards within a few ten of meters to a thick deposit, consisting on an unlaminated organic-rich gelatinous mud that supports the growth of millimeter-scale gypsum granules (Fig. 3A), here referred as gypsooids (after Vogel et al., 2009). With increasing deep, the authigenic sediment becomes less organic-rich and the gypsooids form a coarser chicken wire-like depositional fabric (Fig. 3G).

3. Methods

3.1. Collection of samples

3.1.1. Sediment samples

Two thrombolites (~10 cm × 15 cm) were randomly sampled by hand from the shallow lagoon (0.15 to 0.45 m). A thick microbial mat coating from one of the specimens was collected and its different layers (Fig. 3A) were carefully separated with tweezers and sampled. In addition, the organic sediments in the deepest part of the lagoon (Fig. 3G) were retrieved using a PVC dredging device and sampled. In order to preserve the microorganisms for scanning and transmission electron microscopy all the organic samples were placed in sterile 0.5 ml Eppendorf PCR polypropylene tubes containing filtered lagoon water and aqueous glutaraldehyde to a final concentration of 2% v/v.

3.1.2. Water samples

Water samples were collected directly from the lagoon using a 60-ml sterile syringe. The syringe was then fitted with a 0.2 μm micropore filter through which water was expelled into metal-free polycarbonate screw cap sample bottles. Filtered water samples were collected in duplicate, with one being treated with analytical grade nitric acid (to a final concentration of 10% v/v) for cation analysis and the other left unacidified for anion analysis. Overlying water temperatures and pH values were measured immediately upon collection using a Ross (Orion) combination pH electrode. Total alkalinity was measured in situ by using acid titration.

3.2. Biogeochemical profile

A rough estimation of the non-static biogeochemical zoning of the microbial mat overlying the thrombolites (e.g. Revsbech et al., 1983) was obtained by microsensing the unlithified part of the specimen shown in Fig. 3E, which was growing with an overlying water depth of around 10 cm (Fig. 3D). O_2 and H_2S microsensors (UniSense A/S, Denmark, 50 μm, response time, t90, of ~0.3 s), connected to a picoammeter (UniSense), were simultaneously inserted in the mat via a micromanipulator mounted on a heavy solid stand. Measurements were performed at ambient temperature of ~31 °C in 100 μm increments of vertical depth and recorded by using the computer

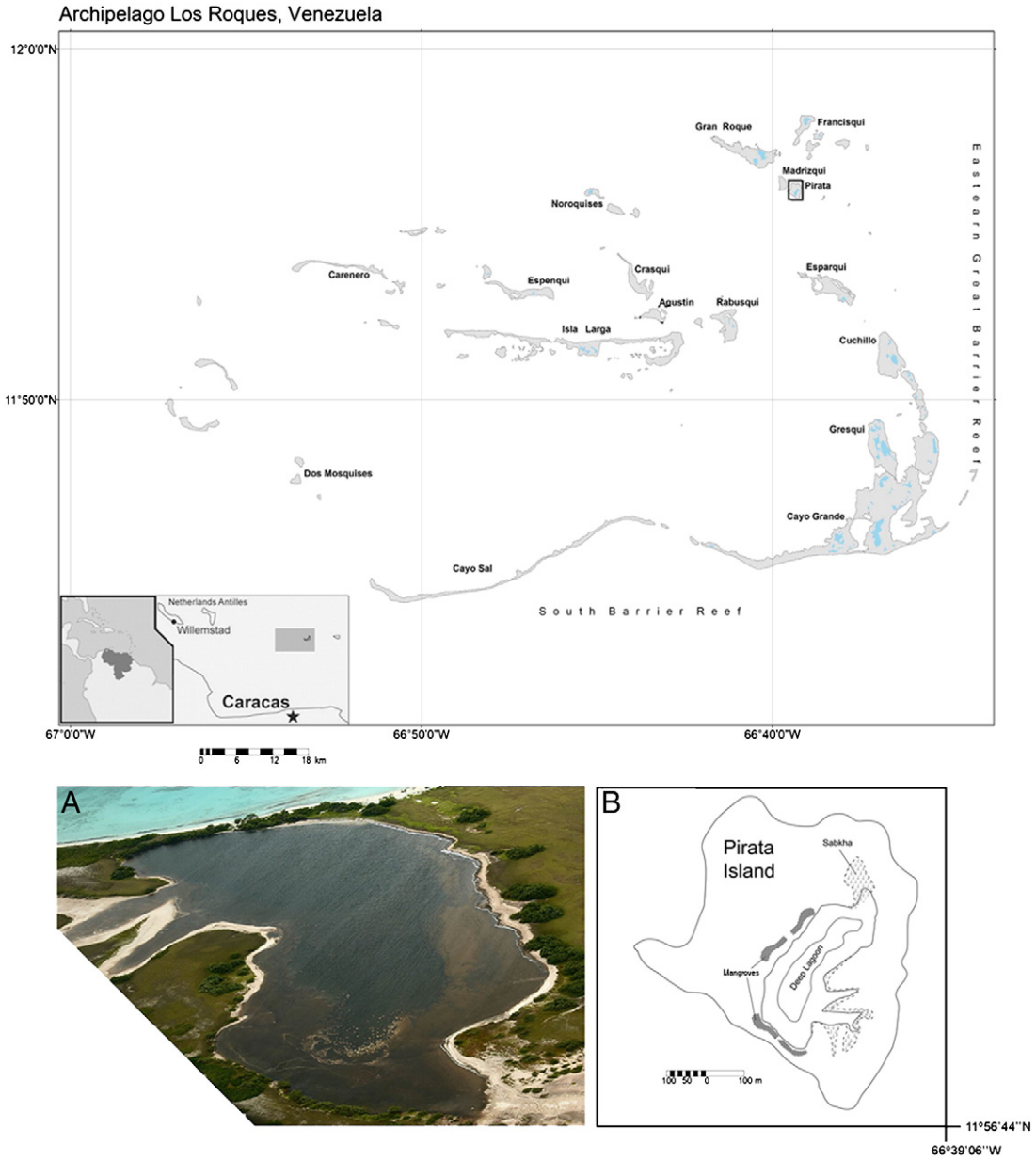

Fig. 1. Location of the study area. Inset A: Oblique aerial view of Laguna Pirata. Inset B: Map of Pirata island.

software Profix (UniSense A/S, Denmark). Prior to the measurements, the O_2 microsensor was linearly calibrated by using picoamperes readings in the O_2-saturated overlying water and in ascorbic acid (0.1 M, for 0% O_2 saturation). The calibration of the H_2S microsensor was performed using a sulfide standard with an ionic strength of 0.5 M buffered to the pH of the overlying water (~9.1).

3.3. Aqueous geochemistry

3.3.1. SO_4^{2-} and Cl^- ions chemistry

Quantitative analyses of SO_4^{2-} and Cl^- anions were performed using a Dionex DX600 Ion Chromatograph (IC) at the University of Alberta. Samples were diluted as required before analysis to reduce salinity to operational values adequate for the analytical machine.

3.3.2. Major and trace metal concentrations

For determination of major and trace metal compositions of the Los Roques lagoon water, the samples were digested with HNO_3 (8 N) and analyzed using a Perkin-Elmer Elan6000 quadrupole ICP-MS coupled to a New Wave UP-213 laser ablation system at the University of Alberta. The ICP-MS instrument parameters were as follows: RF power 1200 W, peak hopping acquisition, 50 ms dwell time. Quantitative results were obtained via calibration of relative element sensitivities against a solution containing 10 ppm of Br, In, and Sc as internal standards. Relative standard deviations (2σ level) were between 3% for Na and Fe, 0.35% for Al and Zn, and between 0.005 and 0.06% for most analyzed elements. Detection limits were between 0.006 ppb (e.g., Mn and U) and 0.75 ppb (e.g., Fe).

3.3.3. Speciation modeling

The degree of saturation of dissolved mineral species in the lagoon water was determined using the geochemical speciation program PHREEQC (Parkhurst and Appelo, 1999). Theoretical speciation results are presented in terms of the saturation index (SI) for predicted minerals, where SI is defined by $SI = \log(IAP/K_{sp})$, with IAP and K_{sp} being the ion activity product of the dissolved constituents and solubility product for the minerals considered, respectively.

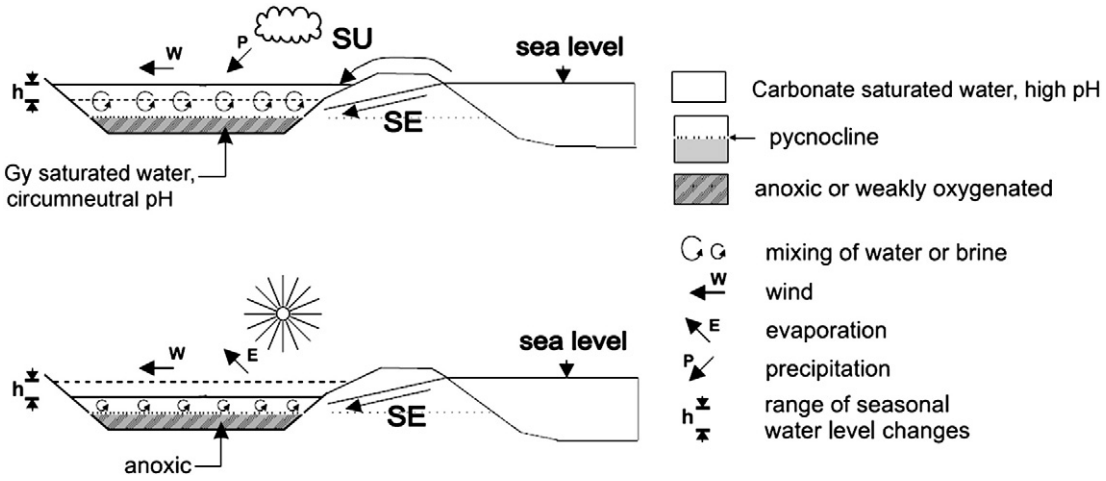

Fig. 2. Schematic hydrological model of Laguna Pirata. SE: seepage seawater influx, SU sporadically, during storm events, surface seawater influx may occur. Adapted from Babel (2004), Fig. 2.

3.4. Solid phase mineralogical/geochemical analyses

3.4.1. Major element geochemistry

We systematically analyzed various levels from the two thrombolite samples for major element geochemistry by electron microprobe analysis (EPMA) after the samples were mounted in epoxy. Wavelength dispersive analyses were conducted using a JEOL 8900 Superprobe (15 kV accelerating voltage; 10 μm beam diameter, and 15 nA current and 30 s counting time). The following mineral and synthetic crystals were used for calibration: F-93(Mg), diopside (Ca, Si), willemite (Mn), Hem639 (Fe), magnesite (Mg), barite (SO_4) and pyrope (Al_2O_3). Analytical precision was monitored through triplicate analyses at each spot area. Data are presented in a 100% carbonate basis.

3.4.2. Trace element geochemistry

The samples analyzed by EPMA were also analyzed for trace element composition by ICP-MS. Quantitative results were obtained via the calibration of relative element sensitivities against the NIST 612 standard with analyses being normalized to [Ca], previously determined by electron microprobe analysis for the unknowns (Jarosewich, 2002). The spot size was 30 μm in diameter, with the averages of least three laser spots reported. Concentrations below the detection limits are indicated where appropriate. Trace elements were determined for the basal, middle, and uppermost crusts of the specimen (for a total of 94 laser spots), and in the authigenic carbonate phases present in the microbial mat coating the same specimen (40 laser spots).

Data reduction and concentration determinations were obtained using the GLITTER® (New Wave Research) laser ablation software. Repeated analysis (n = 6) of the standard yielded relative standard deviations of between 0.01 and 0.5% (2σ level) and detection limits between 0.02 ppm (e.g., Zn, Cd, Cu) and 0.06 ppm (e.g., Mg, Sc, Sr) for most elements (except for elements like, B, Yb, Lu).

3.4.3. Stable C- and O-isotope analyses

In order to evaluate isotopic shifts within the thrombolites, four calcified crusts occurring at different depths within the selected specimen were sub-sampled in duplicate. In addition, ~20 mg of authigenic carbonate grains were carefully picked from freeze-dried biofilm material. The authigenic nature of the mineral components of the mats was determined through the examination of the size, morphology and distinctive optical features of the grains by using reflected light and blue light excitation microscopy (after Dravis and Yurewicz, 1985).

Prior to analysis, the subsamples were treated for 48 h with H_2O_2 (30%) to remove residual organic matter, rinsed three times using ultrapure water, and dried overnight in a vacuum oven at 30 °C. Stable C-isotope analyses of carbonates were performed by immersing whole-rock powders in 100% phosphoric acid while under vacuum (McCrea, 1950) and analyzing the released CO_2 on a Finnegan MAT 252 mass spectrometer at the University of Alberta. The data are reported in δ-notation with respect to V-PDB for carbon and oxygen (Craig, 1957, 1961).

3.4.4. Scanning electron microscopy (SEM)

Thin sections and grain mounts were sputter coated with gold. SEM observations were performed at the University of Alberta on a JEOL JSM-6301FXV instrument, which has an attached Norvar energy-dispersive spectrometer system (PGT). Images were taken at 5 kV, while EDX analyses were done at 20 kV; a constant working distance of 15 mm was used throughout our SEM analyses. The textural relationships between the exopolymeric matrices and their authigenic phases were visualized by using both low-temperature (Cryo-SEM) and the critical point drying methods.

3.5. Biological SEM and TEM

Millimeter-size samples were rapidly frozen by immersion in liquid nitrogen (−200 °C), then introduced in an Emitek K1250 cryo-chamber where they were fractured at −180 °C, superficially sublimated at −90 °C, gold coated at −180 °C, and then introduced in the refrigerated column of the JEOL 6301F at −180 °C to conduct high-resolution examination of internal biofilm structure and mineral/microbe textural features.

In addition to the techniques describe above, the correlative TEM preparatory scheme of Liss et al. (1996) was used to analyze individual portions of the microbial mat that coated the microbialite specimen under examination. Samples were embedded in standard low-viscosity epoxy resin, and subsequently polymerized (Spurr, 1969). The resulting blocks of embedded biofilm were sectioned with a diamond knife mounted in an ultramicrotome (Reichert Ultracut E). Ultrathin sections for morphological studies were cut at 50 to 70 nm and mounted on formvar-covered TEM grids (Marivac Canada) with, and without, counterstaining. Sections of biofilm were observed and images captured in transmission mode using a Philips/FEI (Morgani) Transmission Electron Microscope with CCD camera (TEM-CCD) at an accelerating voltage of 80 kV at the Department of Biology, University of Alberta.

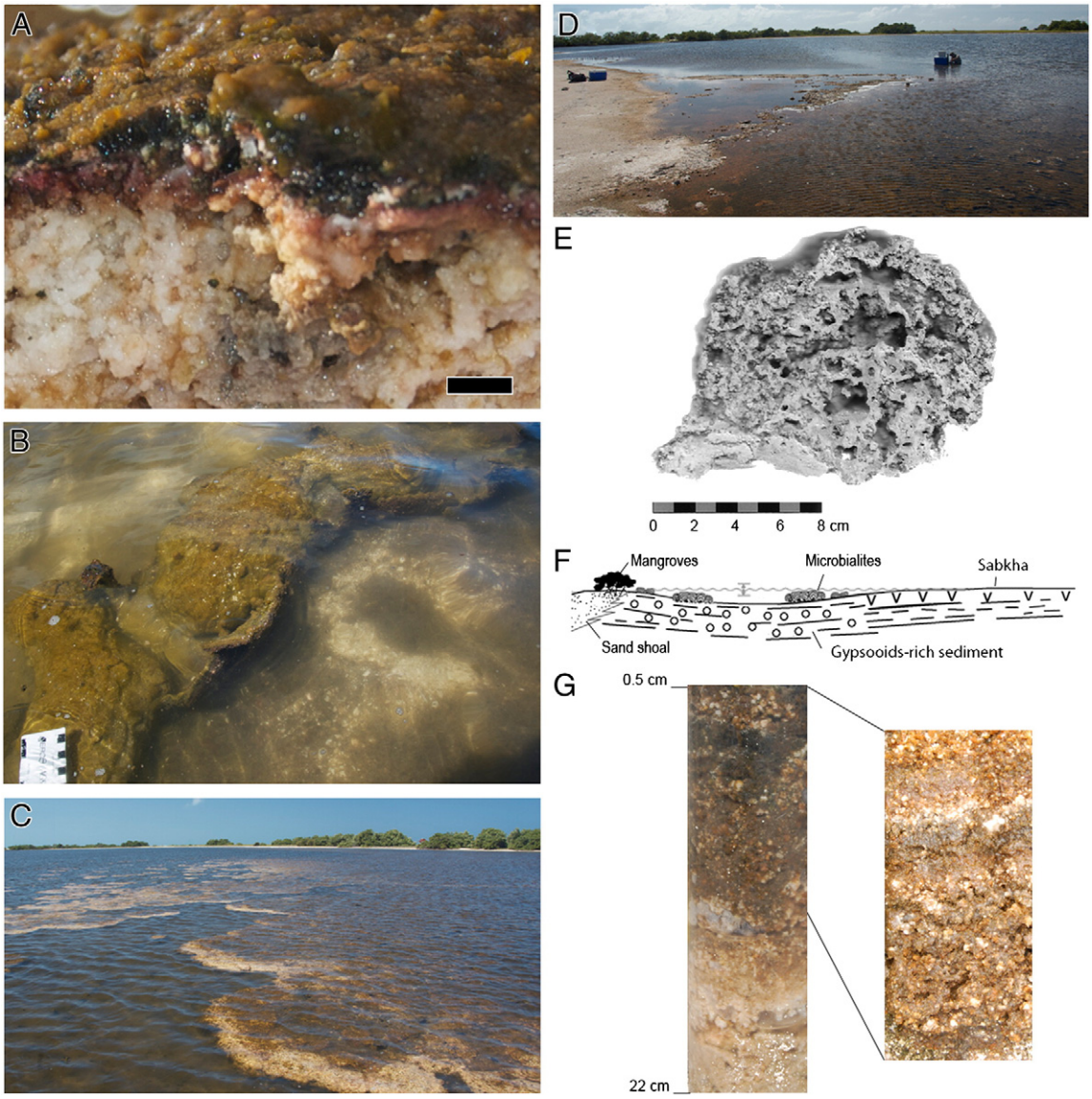

Fig. 3. General macroscopic features of the microbially-influenced sedimentation in Laguna Pirata. (A) Microbial mat coating a thrombolite, the mat exhibit distinctive layering related to vertical array of bacterial communities. Note the masses of microcrystalline gypsum. Scale bar is 10 mm. (B) Close-up of thrombolites, notice microbial mat coating the structures; water depth 10 cm. (C) Dense coalescent growth of thrombolites, water column may vary from 15 cm to 45 cm. (D) In situ microsensing of the bacterial mat; view from the sabkha (E) A collected thrombolites specimen. Note that the thrombolitic fabric (clotted) is dominant over the stromatolitic fabric (laminated zone); more evident in the base of the structure. (F) Distribution of carbonate–evaporite subfacies in Laguna Pirata. (G) The organic-gypsum rich sediment in the deepest part of the lagoon.

4. Results

4.1. Lagoon water chemistry

At the time of the field work (February 2009), measured pH values of the surface waters of Laguna Pirata varied between 8.7 and 9.3. The water temperature fluctuated between 28 and 35 °C and the average salinity was approximately 90‰, reaching up to 140‰ in the adjacent sabkha flat (Fig. 3D). In terms of major ion chemistry the Mg/Ca molar ratio was found to be 6.1, showing that the lagoonal surface waters were relatively enriched in Mg as compared with Los Roques seawater (Mg/Ca = 5.6). Other relevant chemical features of the lagoon water are summarized in Table 1. Laguna Pirata waters are also slightly enriched in Co, Fe, Ni, Mn with regards to mean seawater; conservative with respect to Ti, Cu, Cr, Mo, U and V, and depleted in Zn, Zr, Ti, Nb and Sn (Fig. 4).

The hypersaline superficial waters are oversaturated with respect to dolomite (SI = 3.8), calcite (SI = 1.4), and aragonite (SI = 1.28), whereas gypsum, the most abundant mineral phase in Laguna Pirata, is slightly undersaturated (SI = −0.29). Undersaturation of the surface waters with respect to gypsum may be due to temperature, oxygenation and mixing (e.g., Last and Schweyen, 1983) or its high natural alkalinity (e.g., Thompson and Ferris, 1990).

Table 1
Chemical features of surface Pirata's water. The mean chemical composition of Los Roques seawater (sampled in two different sites in the unrestricted lagoon) is also shown for comparison.

Sample	Ca^{2+} (mmol)	Mg^{2+} (mmol)	Sr^{2+} (μmol)	Salinity (‰)	SO_4^{2-} (mmol)	Total alkalinity (mM/L)
Laguna Pirata evaporated seawater	17.5	108.9	97.12	90	66.8	169
Seawater at Los Roques	10.1	52.2	96.1	40	31.6	134

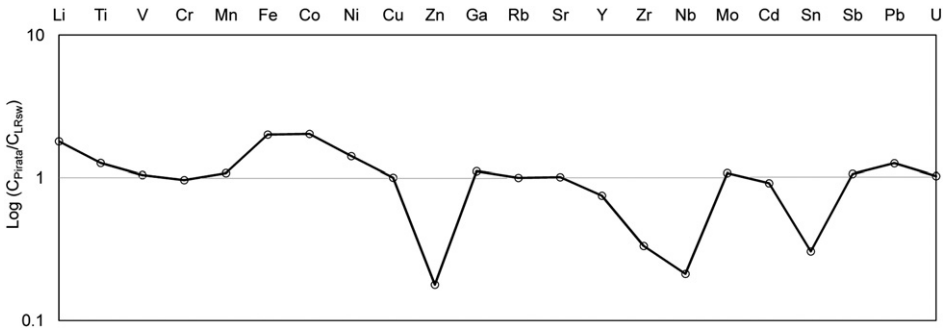

Fig. 4. Logarithmic plot showing the enrichment/depletion factors of selected trace elements in the surface waters Laguna Pirata, normalized respect Los Roques seawater (LR_{sw}).

4.2. Geobiology of the microbial mats

4.2.1. The thrombolite-constructing mat

Microbial mats growing on the thrombolites reach up to 2 cm in overall thickness (Fig. 5A). The uppermost photosynthetic layer consists of a 4 mm thick yellowish to green zone that is dominated by filamentous cyanobacteria (e.g., *Oscilatoria* sp.) and algae (mostly unidentified diatoms) (Fig. 6). During daylight hours, these oxygenic photosynthesizers account for an increase in the partial pressure of oxygen at the water/mat interface from 0.45 to 1.05 atm.

Below the uppermost layer, a green layer extends from 4 to about 10 mm deep within the mat. It contains a high diversity of organisms, ranging from filamentous cyanobacteria, including a sulfide tolerant *Spirulina*-like cyanobacterium to clump-forming non-identified microcolonies of rod-shaped cells (~3–5 μm in diameter) enclosed by multilaminate sheaths (Figs. 6, 7A–C). Solitary *Beggiatoa*-like cells, commonly exhibiting intracellular sulfur accumulations (Fig. 7D, left cell), were also found. In the case of the latter, microsensors data shows that this layer coincides with a zone exhibiting steep opposing gradients of decreasing O_2 and increasing HS^- (Fig. 5B); in this zone, white filamentous laminae (Fig. 5A) are suggestive of elemental sulfur accumulation due to incomplete microbially-mediated oxidation of HS^- (i.e., van Gemerden, 1993).

At depths >10–12 mm, the microbial mat becomes increasingly sulfidic as evidenced by peaks in dissolved HS^- (Fig. 5B). At night, the top of the sulfidic zone shifts upwards. Fine scale microscopy of this layer reveals that it is made up mostly of rod-shaped bacteria encapsulated by EPS. Morphologically the cells resemble some of those occurring in thick EPS in the overlying layer (cf. Fig. 7C and G).

Storm-derived sediment grains are randomly dispersed within the lagoon's microbial mat. The grains are mostly subangular in shape and consist of millimeter-scale fragments of the calcareous algae *Halimeda* sp.; other storm-transported bioclasts, such as ooids and shell fragments, are also present. The allochems are frequently affected by microboring (Fig. 8), which could represent biogeochemical dissolution produced by endolithic microbial communities (i.e., those between and upon mineral grains) (e.g., Kobluk and Risk, 1977; Reid and Macintyre, 2000). Microprobe analysis indicates that Mg-calcite may be formed as an internal microcrystalline precipitates within the microbore cavities; it also occurs as part of a thin microcrystalline cement often encrusting primary grains coated by EPS microfilms (Fig. 8).

As for the inorganic constituents of the thrombolite-constructing mat, calcium carbonate accumulation consists dominantly of crystal clusters (15–25 nm in diameter), which forms small peloids up to a few hundred micrometers in diameter (Fig. 9). Mineralogically, the authigenic precipitates consist of: (1) micrometer-scale aragonite needles usually forming peloidal aggregates of up to 400 μm in diameter (Fig. 9A, B); (2) ellipsoidal aggregates formed by blocky calcite crystals (Fig. 9C); (3) spheroidal forms of Mg-calcite, with grain sizes ranging from 2 μm up to 10 μm and which may, or may not, be calcified bacterial cells and their EPS; and (4) spherical Ca-phosphate particles up to 20 μm in diameter which are encrusted by calcified Mg-rich precipitates (Fig. 9E, F).

4.2.2. The gelatinous gypsooid-supporting matrix

In contrast to its shallower counterpart, the gelatinous organic matrix forming in the deepest lagoon (water depth >1.0 m) lacks a

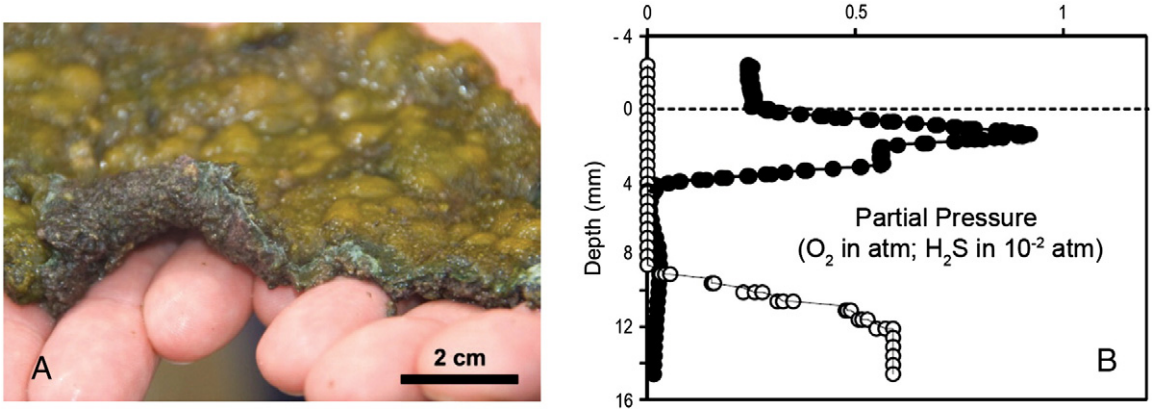

Fig. 5. Macroscopic and microsensing data from the bacterial mat associated with the accreting thrombolitic structures. (A) This bacterial mat was coating the thrombolite specimen shown in Fig. 3E. The upper layer is dominated by cyanobacteria, with algae and diatoms also present; underneath the upper layer, between 4 and 10 mm depth, a purple to green layer can be distinguished, the layer has a white fibrous lamina of elemental sulfur. (B) Daylight microelectrode profile of the bacterial mat shown in (A). The partial pressure of oxygen in the mat/water interface rises dramatically near the surface, from 0.25 to 0.95 atm. From 4 to 10 mm there is a zone of steep opposing gradients of oxygen (from above) and sulfide produced by sulfate reducing bacteria.

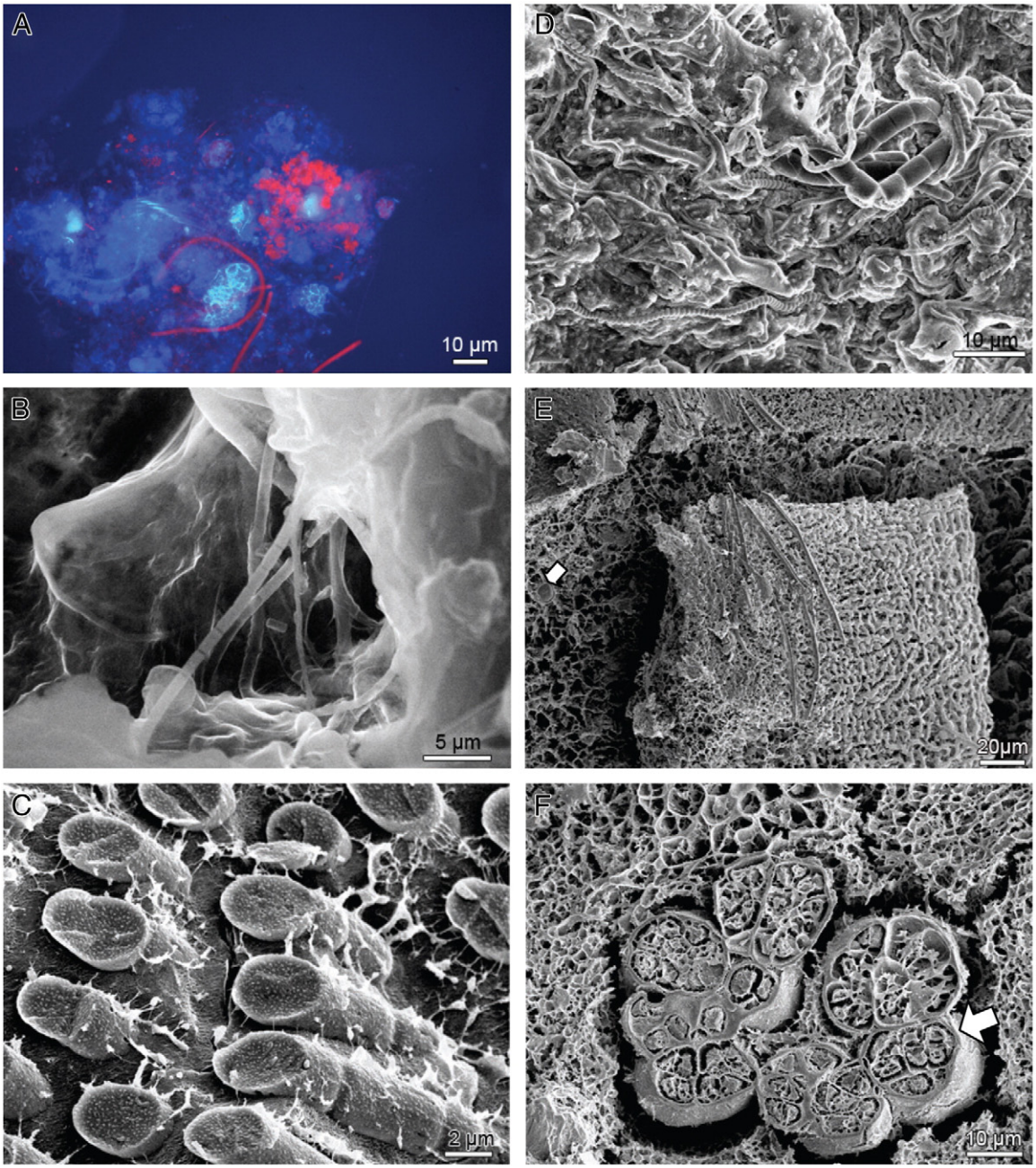

Fig. 6. Delicate microbial features from the biofilm associated with the microbialites of the Laguna Pirata. (A) Autofluorescence in the upper layer of the microbial mat shown in Fig. 4A. Photosynthetic bacteria (red autofluorescence excitation) within an EPS matrix (blue autofluorescence). (B) and (C) Filamentous bacteria (in their amorphous exopolymeric sheath). (D) Middle layer of the thrombolite-constructing mat showing high microbial diversity, spirochetes and other unidentified filamentous bacteria, presumably sulfate tolerant, are evident. (E) Shows abundant coccoid bacteria associated to a filamentous community. The arrow shows a micrometer-scale mineralized spheroid shown in detail in Fig. 9F; bottom layer at the shallow lagoon's mat. (F) Bacterial community from the deepest thick-mat, these rod-shaped bacteria usually form aggregates within a continuous sheath (arrow).

multicolored mat and consists of a non-lithifying, purplish slime of about 30–40 cm thick. The organic matrix material at the hypolimnion is dominated by coccoid bacteria (~2–4 μm in diameter) that resemble those of the Chromatiaceae family (e.g., *Thiocapsa* sp.) (Figs. 6F, 7H) and generally exhibit intracellular S^0 mineralization (Fig. 6H, I). The cells occur singly or in hemispheroidal cell pairs, forming irregularly to ordered EPS-enclosed colonies (2–8, or more cells). Bacterial cells exhibiting similar morphologies were also observed in the suboxic layer of the thrombolite-constructing mat (Fig. 7D), but there they occur in lower population densities (Fig. 6F).

Authigenic gypsum is present at the bottom of the deepest lagoon where it forms centimeter-scale aggregates or gypsooids. The gypsooids are comprised of individual crystals with sizes ranging from 50 to 400 μm (Fig. 10A, B). Petrographical analyses of the gypsooids show that individual crystallites develop mostly as equant-shaped and distorted forms (Fig. 10). In addition, delicate gypsum rosettes were observed in the intracrystalline spaces of the distorted gypsoids. These polycrystalline aggregates were commonly observed coated by EPS, suggesting that their formation is associated with the presence of polysaccharide-rich organic matrix as has been previously demonstrated elsewhere (e.g., Cody and Cody, 1988).

Aragonite is subordinate in abundance to gypsum; when observed, aragonite grows rarely as delicate needles embedded in cracks parallel to the {010} cleavage of the host Ca-sulfate or as peloids exhibiting a

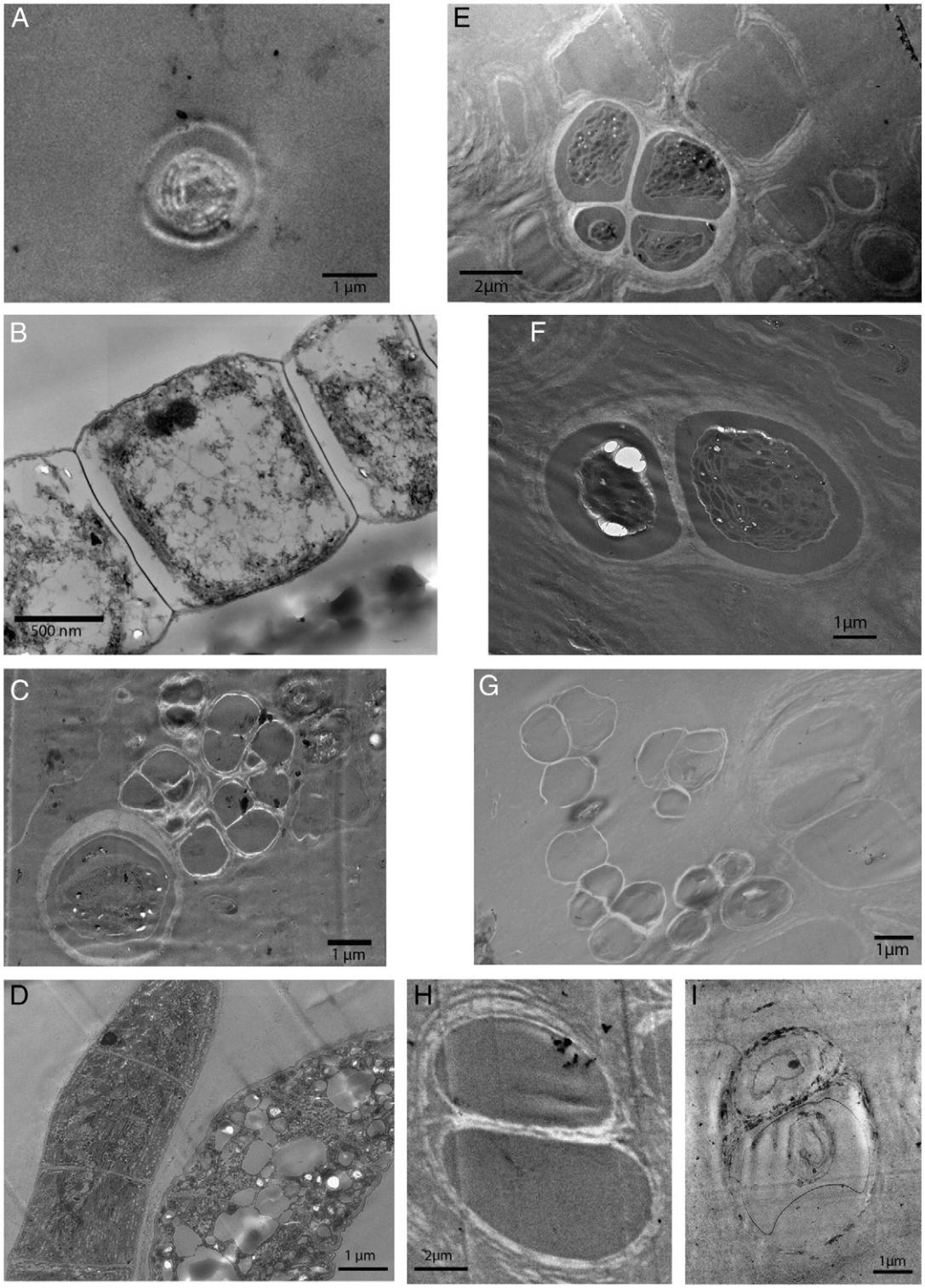

Fig. 7. Transmission electron micrographs (TEM) showing the ultrastructure of microbes observed in Laguna Pirata's mat. (A) *Syenocchochus*-like bacteria in the upper layer. (B) Unidentified segmented filamentous microorganism; upper layer. (C) coccoid purple photosynthetic bacteria showing intracellular sulfur mineralization. Note the association with other diplococci bacterial clumps similar to the ones shown in G (deepest lagoon). (D) A couple of different unidentified anaerobic photosynthetic bacteria from the middle layer. Note distinctive thylakoids-like structures in the left side cell and the abundance of lipids in the right side cell. (E, F) Purple cocci sulfur bacteria with probable affinities to *Thiocapsa* (Buchanan and Gibbons, 1974); bottom layer of the shallow lagoon's mat. (G) Presence of a distinct membrane bounded dense region and the absence of 'thylakoids' suggest that these rod shaped cells are heterotrophs. (H–I): Unidentified microbes from the 'deep lagoon' (H: unstained, I: stained).

radiating arrangement (Fig. 10C, F). A centimeter-scale accumulation of gypsooids sets apart a less-cohesive layer at the top of the sediment column from a relatively more coherent layer at the base (Fig. 3G). The sediment substrate consists of organic-rich sediment exhibiting a chicken wire fabric (Fig. 3G).

4.3. Geobiology of the fossil structures

4.3.1. Mesostructural features

The thrombolites occur as isolated domes arranged sub-parallel to the lagoon shoreline. They range in size from a few centimeters

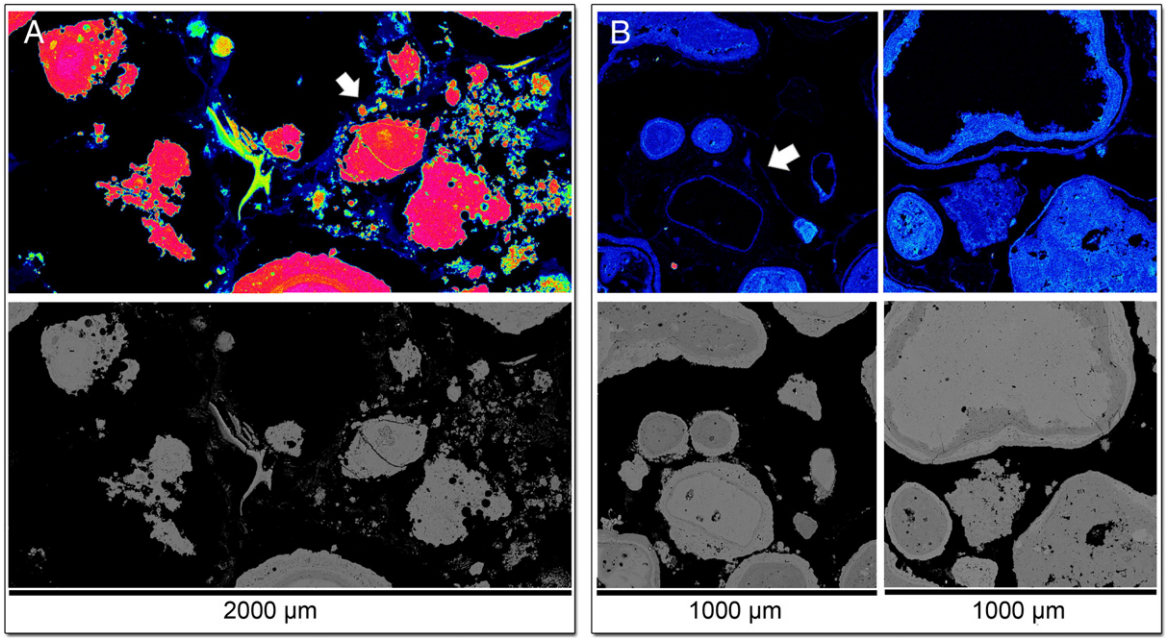

Fig. 8. Microtextural features in sediments from the thrombolite-constructing mat. X-ray maps (CaO (A) and MgO (B)) are shown above; BSE images are shown below. (A) Unfilled microbores and obliteration of authigenic/trapped sediments within the microbial mat. Note the thin EPS coat that serve as the locus of microcrystalline carbonate precipitation (arrow). (B): the X-ray maps (above) show rims enriched in Mg^{2+} that suggest in situ recrystallization. The enrichment of Mg is locally associated to the presence of organic biofilms (arrow). The presence of Mg-zoning in primary carbonate grains suggest that these overgrowths may lead to grain fusion.

to >1 m in diameter, often forming the biggest coalesced structures basinwards. In general, the thrombolites exhibit an internal meso-clotted to crudely laminated fabric similar to what is typically defined as thrombolitic stromatolites (Kennard and James, 1986; Shapiro, 2000; Riding, 2011), but much more porous (Fig. 3E). It is plausible that the cavities associated with the gypsum-dominated framework were formed by entrapment of biomass material followed by its degradation and mineralization.

The local laminar framework consists of isolated, discontinuous, millimeter-thick convex upward zones formed mostly by Ca-carbonates replacing gypsum (Fig. 11). The crude laminar zones intergrade with the dominant grain-supported framework consisting of nodular gypsum cemented by clotted microcrystalline carbonates. Together, these minerals sustain the structural integrity of the thrombolitic fabric. Numerous cavities, up to a few centimeters wide, break up the continuity of the grain-supported framework to yield an overall porosity of 35–40% (Fig. 3E). The larger vugs lack internal sediment; their boundaries are pervasively replaced and cemented by carbonate (Fig. 9C).

4.3.2. Microstructural features

Gypsum accounts for more than 40–55% of the bulk mineralogy. Individual gypsum crystals (c-axis ranging from 200 to 450 μm) are present as mosaics of: (1) equant forms, with well developed *l*{111} prisms; (2) lenticular forms; and (3) distorted tabular habits (Fig. 11). Individual crystals within the gypsum mosaics exhibit randomly oriented optical axes (Figs. 10, 11). Bulk X-ray diffraction analyses (not shown) indicate that the mineral assemblage accompanying gypsum consists of 20–35% aragonite, 15–20% calcite, and 5% halite.

In thin section, 5 to 20% of the calcium carbonate is present as a finely crystalline cement that accumulates in the porous spaces (i.e. Reid et al., 1990), and about 15 to 25% occurs as pseudomorphic aragonite after gypsum. As observed by composite electron S and Ca maps (Fig. 12A, B), the pseudomorphic replacement of gypsum (see below) is typically accompanied by elemental sulfur accumulations, and in areas having a relatively higher pseudomorphic aragonite the content of S^0 increase from less than 1% to up to 5% of the local bulk mineralogy (Fig. 13). As determined by XRD, halite can also be present within these thrombolites. Rare clays were also found present in trace amounts by EPMA. Fabrics formed by microcrystalline carbonates are laminar and clotted/peloidal, the latter forming patches comprised by clusters of finely crystalline cements infilling the interstices between partially replaced gypsum grains (see below) and the framework voids (Fig. 11A, B). Discrete calcified filamentous bacteria occur as tubules that are preserved by occlusion of the mineralized tubules by internal micrite precipitates (e.g., Turner et al., 2000). They appear suspended in the partially replaced gypsum grains, and are more commonly observed at peripheries of gypsum dominated zones and the clotted/peloidal microfabrics (Fig. 11C, F).

Gypsum pseudomorphs. Aragonite, as verified by X-ray diffraction, occurs as a pervasive replacement phase that often mimics the crystalline pattern of gypsum, i.e., it is a pseudomorph (Fig. 9D). Gypsum replacement occurs along crystal boundaries and cleavage/fracture planes. The interface between gypsum and aragonite commonly occurs nearly orthogonal to the dissolution fronts along gypsum crystals (Fig. 9F). Elemental maps show that pseudomorphic crystals are frequently associated with traces of elemental sulfur (Fig. 13).

As determined by laser ablation, strontium in gypsum crystals ($n=23$) approaches concentrations of 995 ± 153 ppm. No inclusion treatment or corrections for celestite were conducted, but only crystals previously identified as gypsum in the microprobe were analyzed by LA-ICP-MS. The Sr content of aragonite replacing gypsum ($n=11$) averaged $4{,}763 \pm 1{,}460$ ppm.

Microcrystalline cements. Backscattered electron images and elemental maps indicate that the cements consist dominantly of Mg-rich micrite with scattered microsparite crystals (approximately 5 μm in size). Microspar crystals form an irregular interlocked mosaic with micritic cements (i.e., Reid et al., 1990) and they often exhibit fuzzy grain boundaries with partially replaced gypsum. The microcrystalline cements form patches in which isolated filamentous and coccoid shapes, of approximately 2 μm in diameter, probably representing mineralized bacteria-like remains, can be distinguished (Fig. 11B).

Although the porosity is typically high, within the crudely laminated zones porosity may decrease to nearly 3% as the fenestral features are progressively infilled by microcrystalline cements. In such

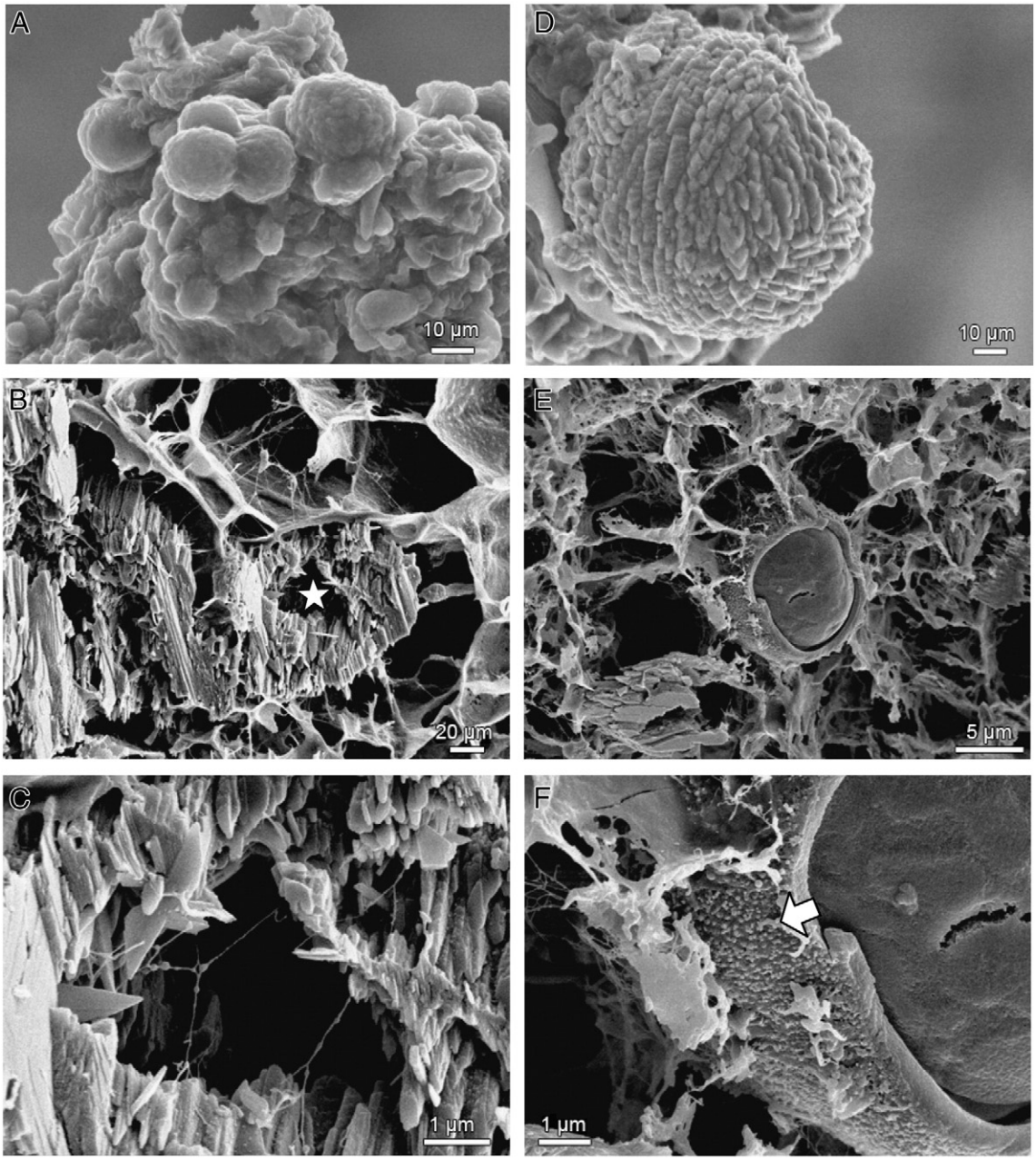

Fig. 9. Cryo-SEM showing authigenic carbonate held by the mat coating the thrombolites. (A) calcite spheroidal aggregates. (B) Aragonite aggregates (peloids) are enclosed by the EPS matrix. The star shows an area amplified in C. (C) The tightly packed peloids show EPS strands crossing the porous spaces of the aragonite aggregates. (D) Detail of a microcrystalline spheroid. Observe the blocky calcite crystallites that compose these spheroids. (E) A solid Ca-phosphate spheroid surrounded by a calcite sheath; EDX analysis revealed that these sheaths are composed of Mg-enriched carbonate. (F) Detailed view of "E", note the presence of nan(n)obacteria-like textures (Folk, 1993) within the sheath surface (arrow).

zones a fine regular micrometer-scale lamination, largely defined by its relative abundance of magnesium, develops to form stromatolitic fabrics that are locally distributed (Figs. 9A, F; 12). By contrast, in gypsum-dominated zones the microcrystalline peloidal cements are more abundant, thus these zone show a clotted thrombolitic fabric (Fig. 9B).

4.4. Carbon and oxygen stable isotopes composition

The oxygen- and carbon-isotopic data for the thrombolites are shown in Table 2. The $\delta^{18}O$ ratios fall between −1.1 and −0.1. The $\delta^{13}C$ ratios range from −8.3 to −2.7. In specimens with two types of carbonates, there exists (1) an isotopically lighter carbonate ($\delta^{13}C = -8.3$ to −5.3‰; $\delta^{18}O = -0.1$ to +1.1‰) replacing gypsum, and (2) a Mg-enriched and isotopically heavier dissolution-enhanced cement ($\delta^{13}C = -2.7$ to −3.2‰; $\delta^{18}O = -0.2$ to −0.1‰). The carbon isotope ratios also partially correlate ($R_S = 0.525$, $p = 0.01$) with the $MgCO_3$ content (weight %). Furthermore, the Mg- and trace metal-contents of these phases seem to correlate with the degradation states of microbial biomass trapped during accretion and areas exhibiting Mg enrichments typically show a significant decrease in the relative abundance of S^0.

4.4.1. Carbon isotopes

Inorganic carbon. Fig. 14 shows the carbon isotopic composition from the lithified and unlithified parts of a thrombolite specimen. A comparison between the average $\delta^{13}C_{inorg}$ values from the unlithified

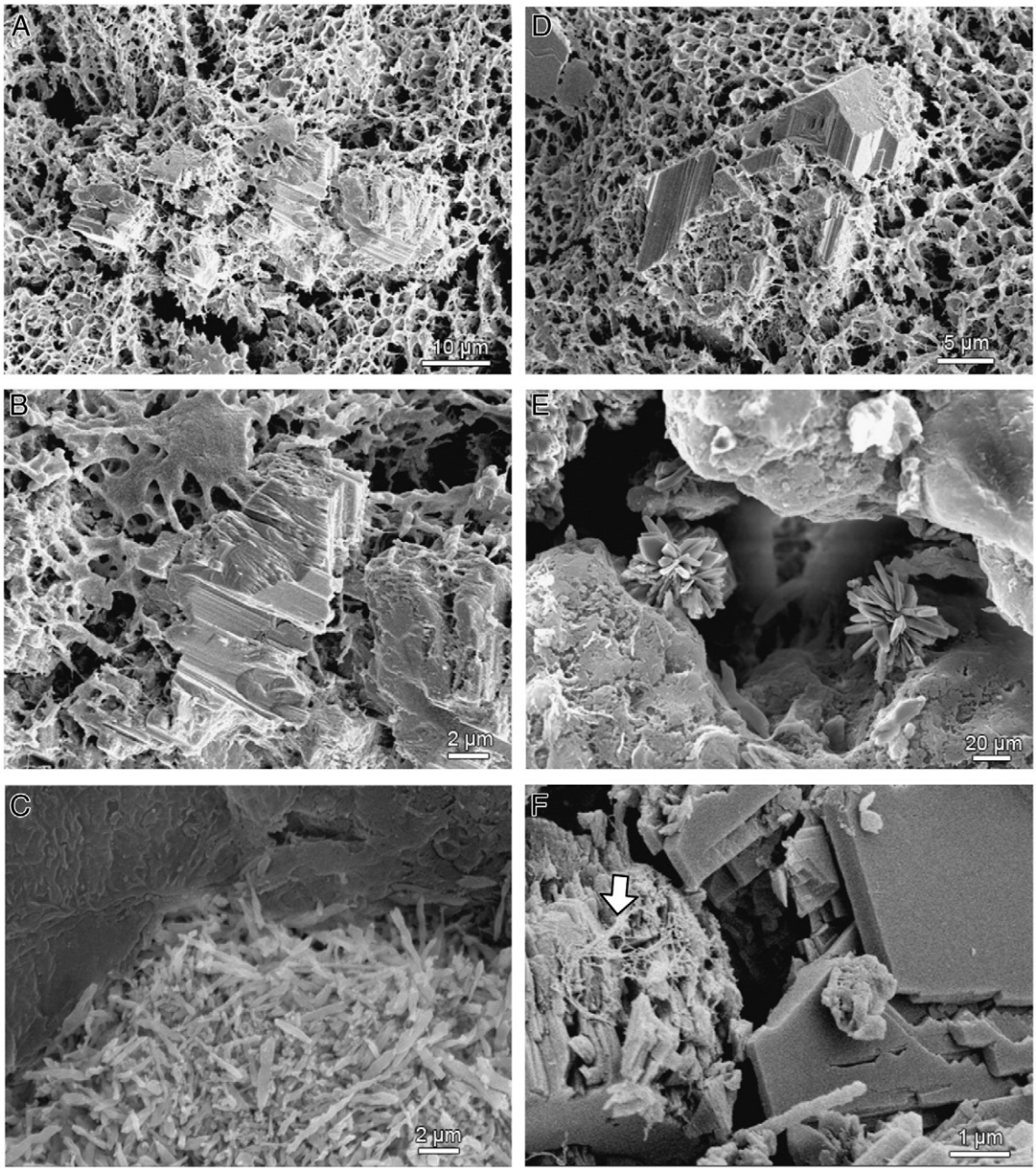

Fig. 10. Biological SEM of theorganic sediment supporting gypsum crystals. Cryo-SEM (A, B, D) and critical point dried (C, E, F) samples showing morphologies of gypsum crystals embedded in the organic slime from the deepest part of Pirata Lagoon. (A) General view of the EPS network. Note subhedral gypsum crystals held in the mucous matrix. (B) Loosely packed subhedral gypsum within the EPS network. Note EPS strands crossing the porous space. (C) Gypsum crystal surface exhibiting a replacement feature composed of randomly oriented bladed aragonite (lower part of the photomicrography). (D) A subhedral lenticular gypsum, the prisms faces {110}, {010}, and {111} are present. (E) Gypsum rosettes crystallized within the fibrous spaces of the crystal aggregates shown in "D". The individual "petals" of these rosettes are lenticular crystals with minor twinning. (F) A plate-like aggregate with minor twin formation. These crystal aggregates are arranged sub-parallel to {103}, the face {111} is also present. The arrow shows fibrous interstitial aragonite.

mat ($\delta^{13}C = -6.1 \pm 1.0‰$) and the cements stabilizing the structure ($-5.4 \pm 2.5‰$, Table 2), shows that the heavier values occur on the initial accretionary surfaces at the base of the lithified thrombolite. On the other hand, $\delta^{13}C$ values of subsamples taken at the center of the specimen (-7.8 ± 0.2) are about $-2.8‰$ lighter than those at the thrombolite's interface, the last in turn are slightly heavier than that of the authigenic carbonates precipitated in the mat (Fig. 14). These values suggest that towards the center there is an additional input of isotopically light carbon to the local pore-water reservoir, probably associated with heterotrophic decomposition of organic material trapped during accretion.

For comparison, Table 2 shows the isotopic ratios obtained for dispersed *Halimeda* sp. flakes fragments trapped by the microbial mat in the shallow lagoon. The $\delta^{13}C$ of the *Halimeda* sp. bioclasts averaged $+2.1 \pm 0.25‰$. The ^{13}C content of calcareous algae usually reflects significant metabolic effects and thus may exhibit a wide range of $\delta^{13}C$ values (Lee and Carpenter, 2001); this variability, however, was not observed in the carbonates cements stabilizing the thrombolite.

Organic carbon. The organic carbon isotopic composition ($\delta^{13}C_{org}$) of the purple layer (Fig. 5) averaged a value of $-15.6 \pm 0.9‰$ (V-PDB). Accordingly, the magnitude of the isotopic shift during organic to inorganic carbon fixation within the specimen under examination, $\Delta\delta^{13}C_{Org\text{-}Inorg}$, is estimated in about 10‰. Such fractionation factor is consistent with the preferential removal of ^{12}C by the microbial biomass.

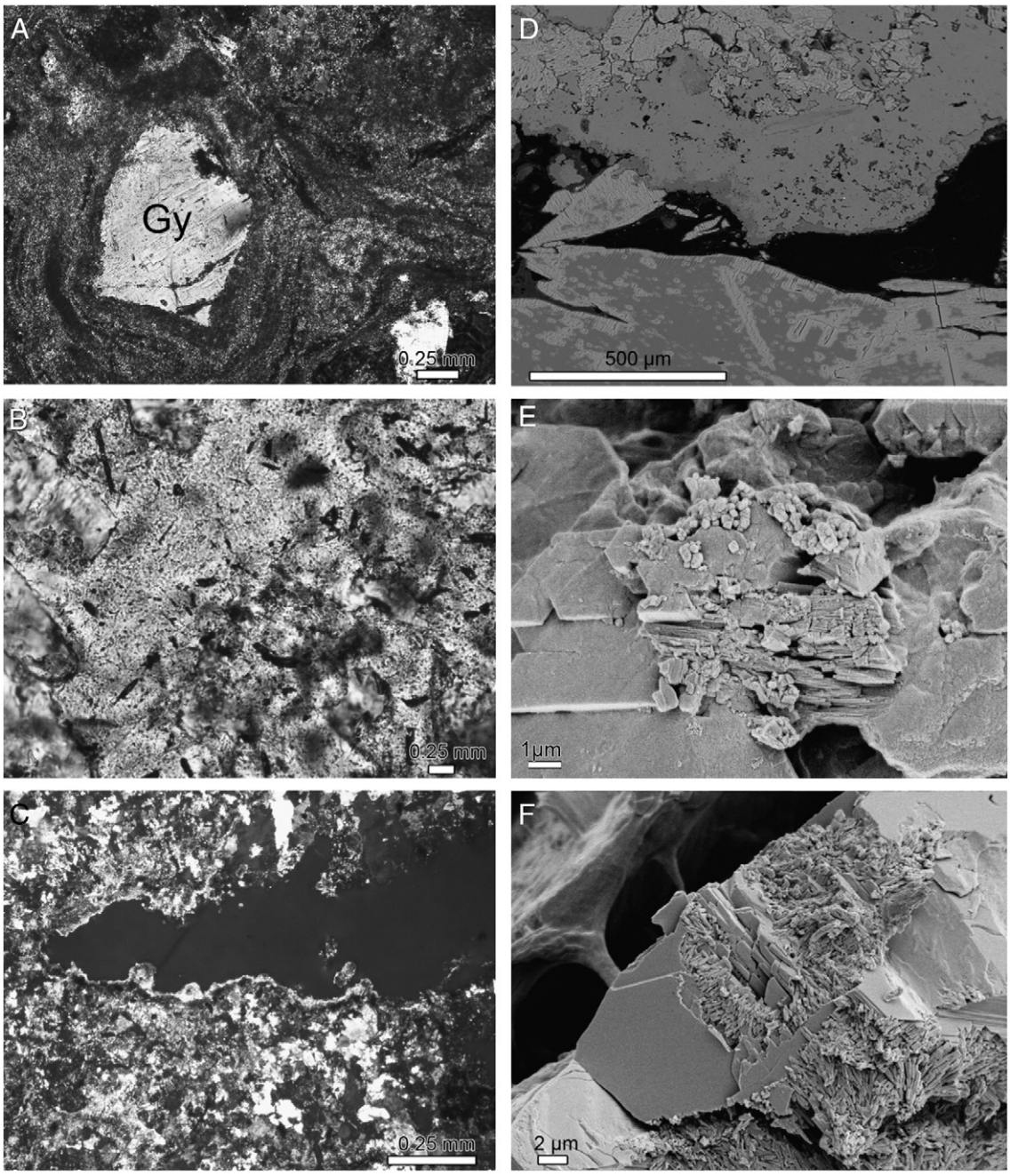

Fig. 11. Replacement of gypsum by carbonate. Microcrytalline cements can be found infilling inter- and intragranular spaces. Standard (A–C), backscattered electron (D) and SEM (E, F) petrography. (A) Base of the thrombolite, the image shows a subhedral, corroded, gypsum crystal (Gy) draped over by concentric micrite/microspar laminae. (B) Micrite/microsparite aggregates around corroded and partially dissolved gypsum crystals. Dark areas dominantly represent accumulation of organic material. (C) Irregular fenestral void enclosed by clotted-laminated micrite/microspar cements. (D) Calcification of gypsum leads to the formation of pseudomorphs. In the pseudomorphs, calcite replacement mimics the {001} crystallographic planes of gypsum although calcification appears to preferentially occur perpendicular to {010} cleavage of gypsum, preserving the (010) cleavage surface. (E) Poikilotopic gypsum enclosed by Mg-enriched cement. F: Solution fronts on gypsum crystals often show aragonite crystals sub-perpendicularly orientated to the gypsum surfaces.

4.4.2. Oxygen isotopes

The mean $\delta^{18}O_{PDB}$ (0.4 ± 0.14‰) of carbonates from the thrombolite are comparable with the values observed in the authigenic carbonates from the living mat, -0.9 ± 0.25‰ (Table 2, Fig. 14). Such values contrast with the mean $\delta^{18}O_{PDB}$ of the trapped *Halimeda* sp. flakes, $+2.2 \pm 0.13$‰. The narrow range of $\delta^{18}O$ values in *Halimeda* sp., which is known to be relatively stable (Lee and Carpenter, 2001), reflects values close to the predicted for equilibrium with Los Roques's seawater and is considered to represent the baseline for the $\delta^{18}O$ value of the bioclast material precipitated in equilibrium with seawater from the unrestricted setting, as such trapping seems to contribute marginally to microbialite accretion.

From the temperature range measured in situ (28 to 35 °C), and by using the equation of Friedman and O'Neil (1977) with a fractionation factor calculated as described in Faure (1991, p. 351), the lagoon water from which carbonates precipitated yields $\delta^{18}O_w$ values between $+1.8$‰ and $+3.8$ (SMOW). The oxygen isotopic values (V-PDB) of the samples are consistent with carbonate phases precipitated in isotopic equilibrium with the lagoon's partially evaporated seawater in a relatively humid setting.

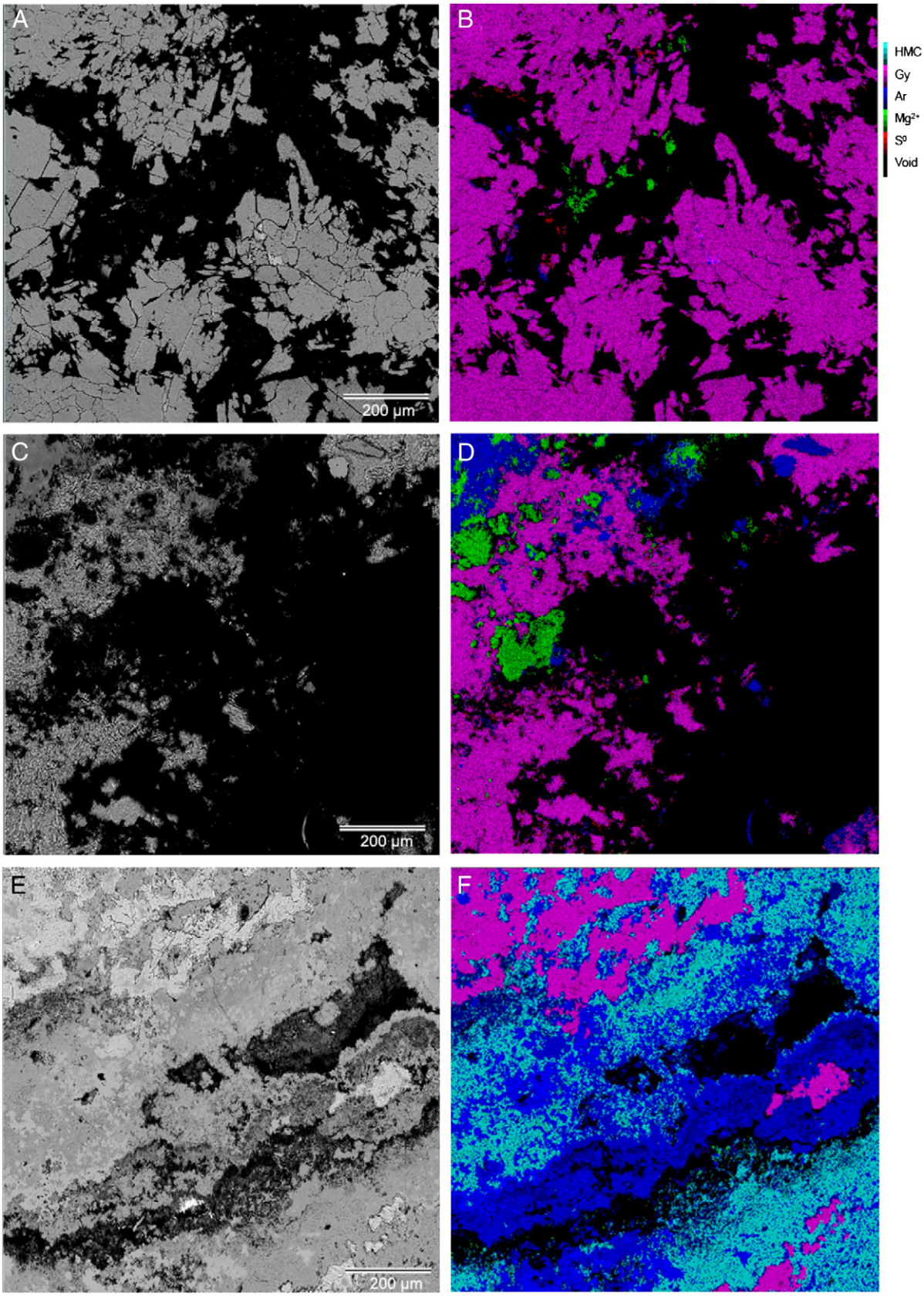

Fig. 12. BSE and composite X-ray maps (S, Mg and Ca) of different zones of the thrombolite specimen examined. (A–B) approximately 2 cm from the top of the structure; (C–D) approximately 7 cm from the top of the structure. (E–F) at the laminar basal part (~12 cm from the top) of the structure. Note S^0 and Mg^{2+} accumulations in B and D and the relative abundance of Mg-rich calcites towards the base (F).

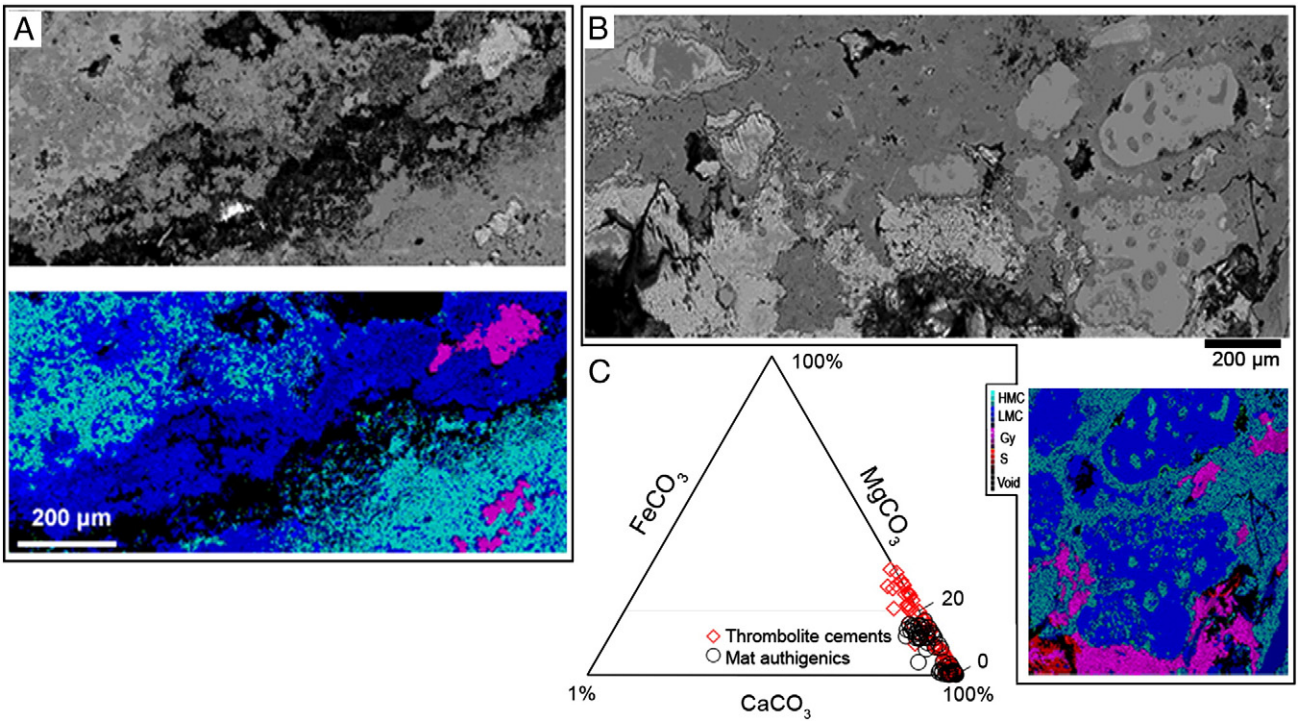

Fig. 13. BSE and X-ray map of the basal part of the thrombolite specimen.(A) fine scale lamination, largely defined by the relative abundance of magnesium (darker areas in the bottom image). (B) BSE and X-ray may show Mg-enriched zones and its textural relationship with aragonite (darker areas in the bottom image). The arrow shows infilled microborings-like as observed in the lower lithified carbonate crusts. (C) Quantitative compositional data (mol%) for calcite cements and mat authigenics. The cements are Mg-enriched relative to the mat's authigenics.

4.5. Trace elements

Table 3 shows the enrichment factors of some minor and trace metals incorporated into carbonates from one lithified thrombolite specimen as compared with the authigenic carbonates from the associated microbial mat. There are striking similarities between the trace metal patterns of the carbonates providing structural integrity to the thrombolites and the trends exhibited by the authigenic fraction precipitated at the mat (Fig. 15), suggesting a common mechanism of trace element incorporation operating in both lithified and non-lithified zones of these microbialites.

Carbonates within the lithified structures are slightly enriched (up to 2×) in Li, Na, V, Cr, Fe, and Pb. Enrichment factors are higher for V, Co, Sb, U (2× to 4×), while Cu and Mo are concentrated between 7× and 12×. Ni exhibits a conservative behavior and its concentration in the authigenic carbonates within the mat match those values observed in the thrombolites. A high-resolution minor and trace element analysis of the thrombolite specimen is shown in Fig. 16. An increase in redox-sensitive elements approximately 6–8 cm below the mat/thrombolite interface is indicative of the local occurrence of more strongly reducing redox microenvironments as reported elsewhere (e.g., Tribovillard et al., 2006), and accounts for the maximum oxygen diffusion zone within the porous fabric.

Table 2
Stable C and O isotopes values from Los Roques microbialites (V-PDB), together with its Mg oxide content (wt. %). *Halimeda* sp. values are shown for comparison. See Fig. 14A for approximate location of the subsamples within the thrombolite.

Subsample	Location	MgO	$\delta^{13}C$	$\delta^{18}O$
1a	Base	21.51	−2.70	−0.10
1b	Base	20.40	−1.93	−0.55
2	Base	7.82	−3.20	−0.20
3a	Middle	4.35	−7.40	−0.10
3b	Middle	6.00	−8.36	−0.10
3c	Middle	5.36	−7.70	−0.55
4	Interface	1.94	−5.30	−1.1
5a	Mat auth	4.81	−5.05	−0.60
5b	Mat auth	6.55	−7.17	−1.14
6a	*Halimeda* sp. Open lagoon	N/D	1.75	−3.05
7a	*Allochem. (Halimeda* sp.)	N/D	2.44	−1.51
7b	*Allochem. (Halimeda* sp.)	N/D	2.42	−1.54
7c	*Allochem. (Halimeda* sp.)	N/D	1.70	−1.92

5. Discussion

As discussed below, the dynamics of phototrophic and heterotrophic bacteria, together with local environmental factors such as the availability of accommodation space and hydrodynamics of the depositional settings, exert a strong control over the growth, mineralogy and fabric of the thrombolites in Laguna Pirata (i.e., Des Marais, 2003). The carbon isotopic signatures, as well as the minor and trace element distribution, within these structures may have relevance for better interpreting the mechanisms by which ancient thrombolites may have formed.

5.1. Accretion model and mineral paragenesis

The accretion of microbialites, in general, is a process sensitive to external or internal influences (e.g., Feldmann and McKenzie, 1998; Andres and Reid, 2006; Planavsky and Ginsburg, 2009), and even small changes in the local environment can yield notable ecological effects, including the reorganization of the entire microbial mat system (i.e., Gerdes et al., 2000; Des Marais, 2003). In this regard, the thrombolites in Laguna Pirata likely reflects a period of gradual lagoon water level decline which results in slow accretion, mostly linked to authigenic carbonate accumulation in the mats, that forms stromatolitic fabrics. As the structures reach the maximum water level, accommodation decreases and vertical accretion is substituted by lateral accretion forming the coalesced meter-scale thrombolites described herein.

Concomitant with mineral authigenesis, the motile photosynthetic microorganisms comprising the mat migrate vertically in order to

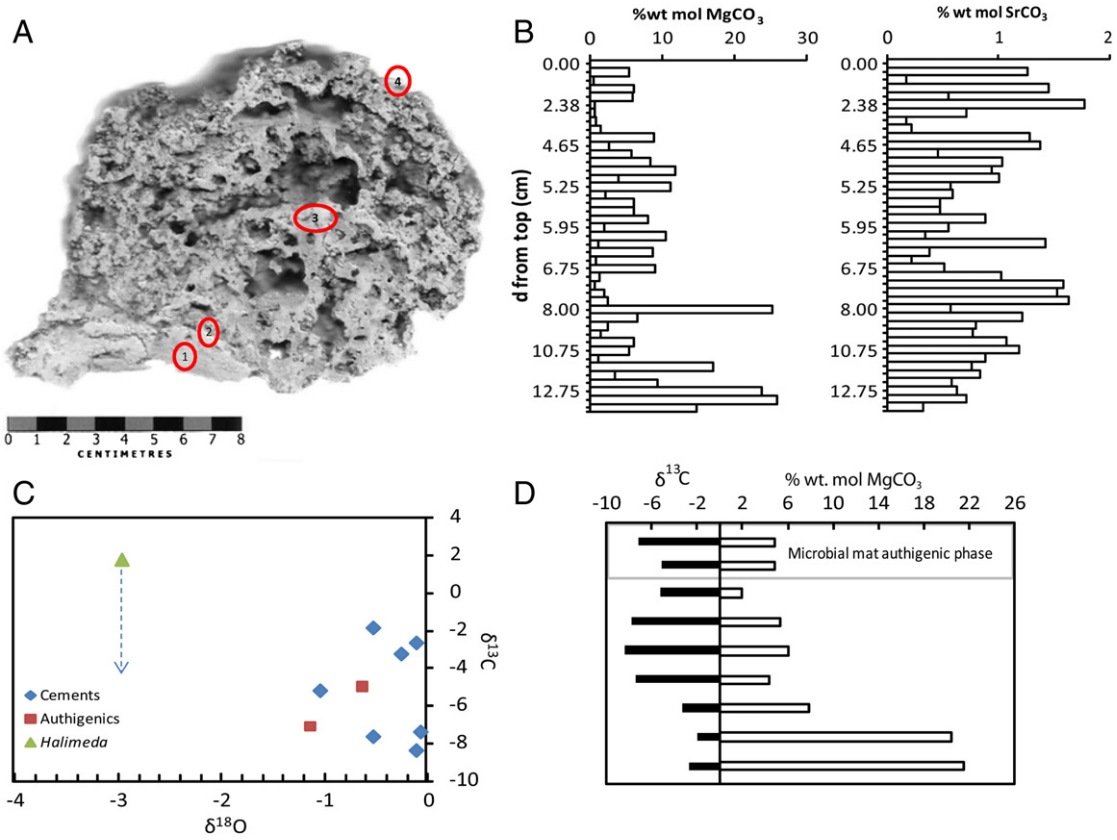

Fig. 14. Carbon and oxygen stable isotopes and major element distribution in one of the specimens collected. (A) Sub-sampled zones for isotopic analysis within the specimen. (B) Down-depth molar variation of $MgCO_3$ and $SrCO_3$ as obtained by LA-ICP-MS. (C) The $\delta^{13}C$ versus $\delta^{18}O$ plot differentiates microbial carbonate from aeolian transported *Halimeda* sp. fragments. (D) Carbon isotopic data with depth in the specimen; a strong positive correlation was found to exist between the average $\delta^{13}C$ values and the $MgCO_3$ content of both microbial mat carbonates and the thrombolite cements.

access zones of optimal light conditions (Buczynski and Chafetz, 1993; Grotzinger and Knoll, 1999; Des Marais, 2003). As primary producers migrate upwards and away from the lithified substrate, the pore-water composition in the space formed between the detached photosynthetic mat and the thrombolite surface then becomes temporarily controlled by the activity of anoxygenic sulfide oxidizers. Their metabolic activity induces physicochemical conditions that lead to fast gypsum growth and further cementation that favor the development of the mososcale thrombolitic fabric. Because the gypsum exhibits distorted and equant forms, it is thought that the precipitation and growth of the primary sulfate crystals occurred under the influence of organic EPS matrices (e.g., Cody and Cody, 1988; Cody and Cody, 1991; Vogel et al., 2010).

Table 3
Comparison of trace elements concentrations of the authigenic carbonates in the microbialites and in the mat.

Element	Average concentration (ppm) in thrombolite cements	Average concentration (ppm) in mat authigenic samples	Degree of enrichment	Degree of depletion
Li	4.1	2.4	1.7	
Na	6,603.4	5,584.2	1.2	
Ti	171.9	177.2	–	–
V	3.0	1.6	1.9	
Cr	12.8	10.7	1.2	
Mn	7.7	9.0		0.9
Fe	124.4	79.1	1.6	
Co	0.9	0.2	3.6	
Ni	1.7	1.7	1.0	
Cu	0.008	0.001	7.6	
Zn	10.9	4.9	2.2	
Sr	5,389.3	4,585.3	1.2	
Y	0.3	0.4		0.6
Zr	0.4	0.4	–	–
Nb	0.1	0.1		0.6
Mo	3.6	0.3	12.2	
Cd	0.3	0.4		0.9
Sn	0.8	1.1		0.7
Sb	0.4	0.1	2.6	
Pb	1.0	0.6	1.6	
U	5.2	2.1	2.5	

As the EPS trapped within the gypsum crystals are partially degraded by endolithic sulfate reducers, which facilitates an increase in pore-water pH (Slaughter and Hill, 1991), the precipitation of 0gypsum is progressively inhibited because the alkalinisation reactions decrease the saturation state of gypsum (Sonnenfeld, 1984; Cody and Cody, 1988; Thompson and Ferris, 1990; Cody and Cody, 1991; Doğanp et al., 2004; Vogel et al., 2009, 2010). Concomitantly, these conditions lead to the early replacement of gypsum by aragonite (Sonnenfeld, 1984; Thompson and Ferris, 1990; Cody and Cody, 1991; Amjad, 1996; Vogel et al., 2010) as the high magnesium concentrations in the pore-water exerts an inhibitory effect over 3precipitation of calcite (Peckman et al., 1999):

$$CaSO_4 \cdot H_2O + 2(CH_2O) + 2OH^- \rightarrow HS^- + CaCO_{3(aragonite)} + HCO_3^- + 3H_2O \quad (1)$$

Local extracellular accumulations of S^0 seems to be associated to pseudomorphic gypsum replacement, suggesting that the replacement process involves the coupled activity of sulfate reducing bacteria (SRB) and sulfide oxidizing bacteria (SOB) (Kah et al., 2001; Visscher

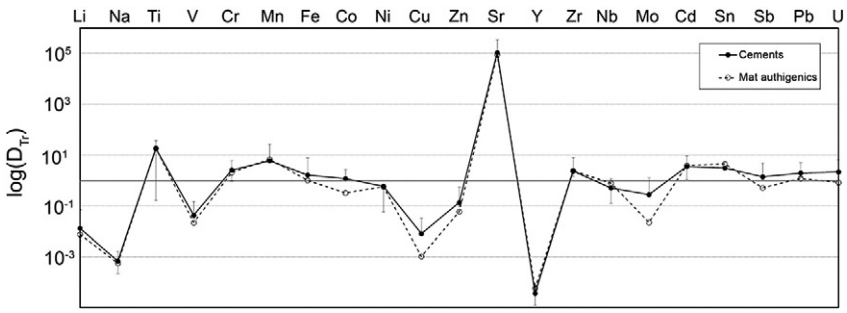

Fig. 15. Logarithmic plot showing relevant metal-enrichment/depletion trends between carbonates phases. We calculated the sediment enrichment/depletion factors by comparing the ratio of the concentration of elements of interest (Tr) and Ca relative to their concentration ratios as observed in the overlying partially evaporated seawater.

and Stolz, 2005; Fernández-Díaz et al., 2009; Vogel et al., 2009). Dissolved sulfide from reaction 1 may partially diffuse upwards and become chemically oxidized by O_2, which was formed within the cyanobacterial layers of the mat:

$$2HS^- + 0.5O_2 \rightarrow 2S^0 + H_2O \quad (2)$$

Reaction 2 leads to the characteristic elemental sulfur lamina that are often observed underlying the cyanobacteria and overlying the purple anoxygenic photosynthesizers (see van den Ende and van Gemerden, 1993; van Gemerden, 1993; Stefess et al., 1996 for details) (Fig. 17).

In addition, by forming dissolved sulfide and contributing to the formation of ammonia, the activity of SRB drives important changes in pore-water alkalinity, pH and metal activities within the thrombolite itself (Slaughter and Hill, 1991; Dupraz and Visscher, 2005; Wright and Wacey, 2005; Decho, 2010). Increased alkalinity leads to an increase in the activity of the Mg and carbonate ions (Berner, 1975) which co-precipitate with dissolved Ca to form Mg-enriched calcite phases that form mostly as microcrystalline cements, but may locally replaces the metastable aragonite precursors (Fig. 17). Importantly, the early diagenetic microcrystalline cements provide structural coherence to the porous structures. A potential outcome from the ongoing diagenetic process is the total occlusion of the porous spaces by secondary carbonate cements and the complete calcification of primary sulfates. This may result in mesoclots separated by patches of mudstone and sparry cements, which, as discussed in the next section, have bioactive metal enrichment trends that correlate well with the degradation states of the organic matter trapped during accretion.

Interestingly, the thrombolites do not occur in the deep portion of the lagoon (water column > ~1 m) where sedimentation consists of chicken-wire gypsum nodules growing in a organic matrix that lacks carbonate cementation. In this zone, tidally-controlled seepage influx and scarce light penetration lead to stratification of the water column, which in turn prevents the development of photosynthetic microbial mats in the deepest part of the basin. As a consequence, the cascade of catalytic reactions controlling the accretion and lithification of sediments in the shallow lagoon realm do not take place, and the H_2S produced in the bottom sediment can be oxidized to elemental sulfur and sulfate (Canfield et al., 1993; van Gemerden, 1993; Kaufman et al., 1996; Visscher and Stolz, 2005) that rapidly react with excess Ca^{2+} ions in solution leading to bottom water gypsum supersaturation.

5.2. Chemical signatures

The degradation of the EPS releases to the pore-waters a number of redox sensitive bioactive elements that were previously sorbed to the functional groups of the trapped microbial biomass (e.g., V, Cr, Mo, Co, etc.; Hunter et al., 1998). Upon release, some of these metals form hydrated complexes with the reactive calcite surfaces and become incorporated into growing carbonate cements throughout a variety of mechanism enhanced by increased alkalinities (see Brand, 1994 for details). This process can lead to localized enrichment trends

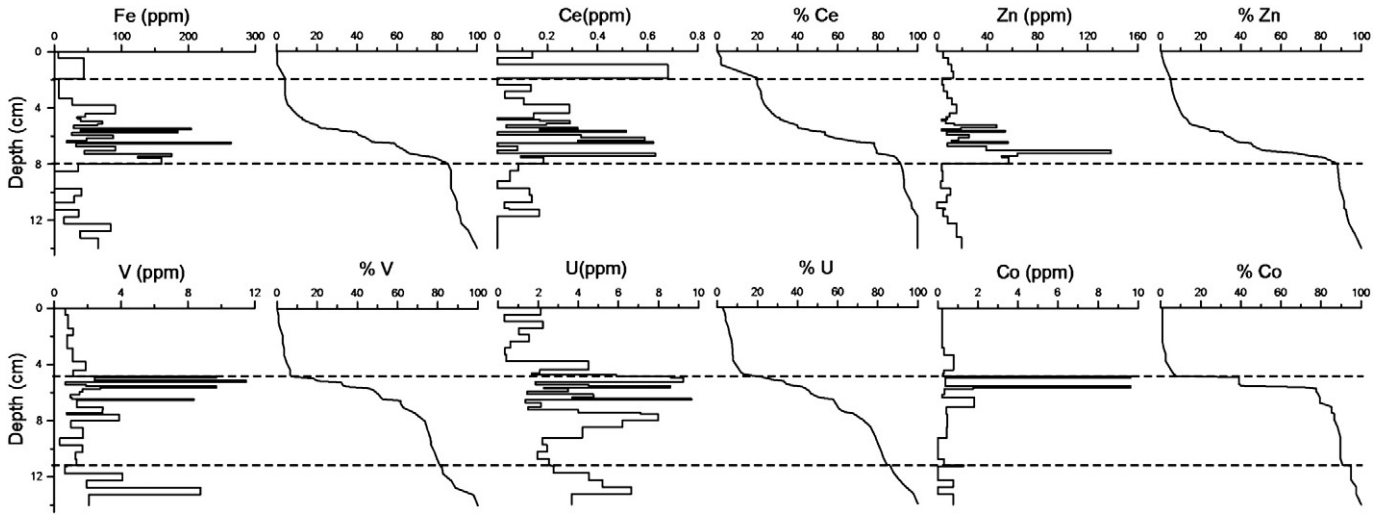

Fig. 16. Summary of relevant vertical enrichment trends within the specimen under examination. The covariance of certain metals within the vertical profile can be interpreted in terms of the microbial process involved in local metal enrichments. To the right of each elemental contour there is an accumulative % vertical profile showing a striking enrichment towards the center of the specimen. See text for details.

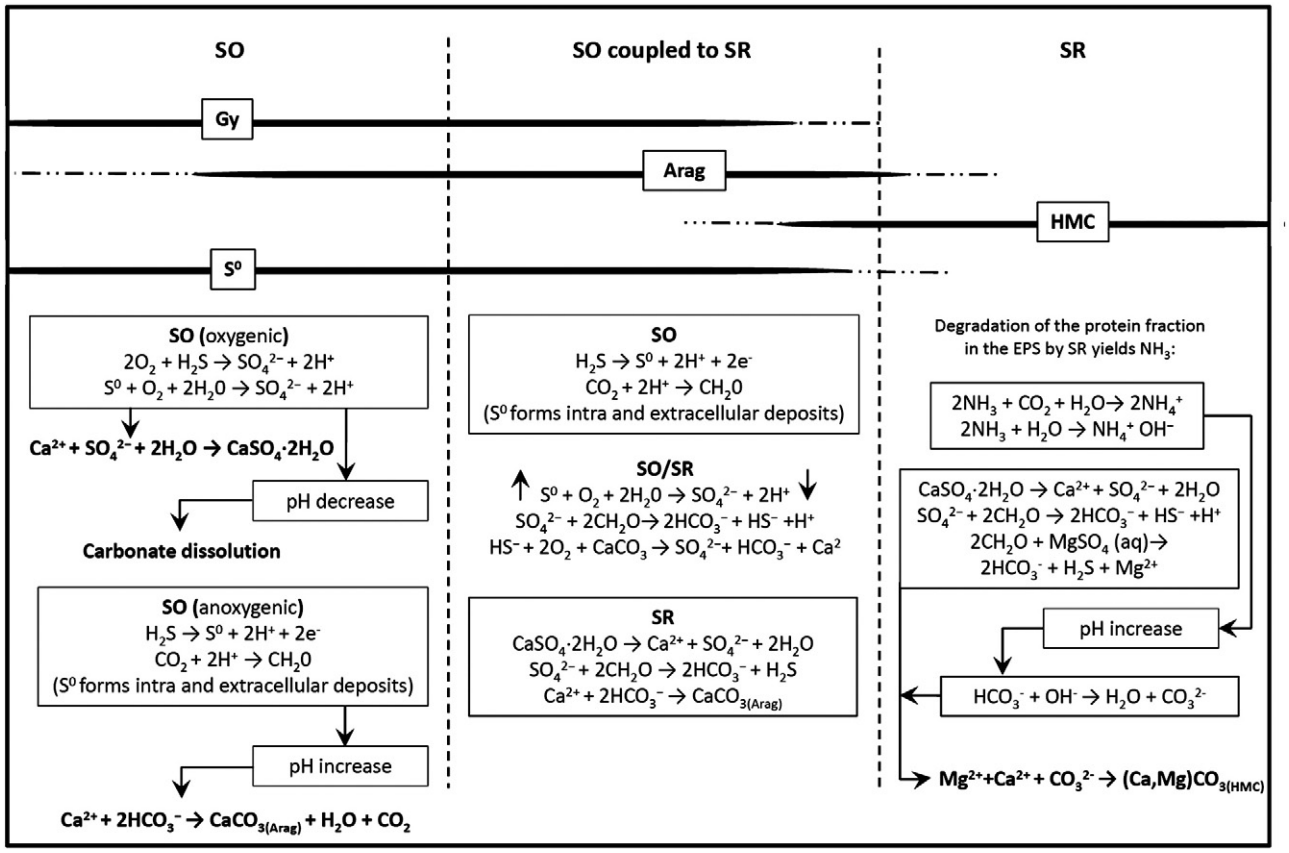

Fig. 17. Paragenetic diagram and relevant metabolic pathways determining mineral associations within Pirata's thrombolites. SO: sulfide oxidation; SR: sulfate reduction; Arag: Aragonite; HMC: High-Mg Calcite.

that are consistent with the availability and degradation states of the organic matter within the structures (Fig. 16).

Similarly, the carbon and oxygen isotopic composition of the carbonate phases within the thrombolites reflect the timing of precipitation and the interplay of organic and inorganic carbon reservoirs; early-diagenetic carbonate cements (average $\delta^{13}C_{PDB} \approx -2‰$) are close to equilibrium with respect to inorganic carbon, whereas deeper in the thrombolites, gypsum-replacing carbonates are relatively enriched in ^{12}C (average $\delta^{13}C_{PDB} \approx -5‰$), likely incorporating carbon released by SRB heterotrophy of organic matter (Fig. 14). The uniformity of the $\delta^{18}O$ values, as compared with allochemical grains in the basin (aeolian-transported *Halimeda* sp. flakes, $\delta^{18}O_{SMOW} = -3.0‰$, Fig. 14), suggests that authigenic microbially-induced precipitation exceeds allochemical trapping and neomorphism.

The lack of correlation between carbon and oxygen isotopes (Fig. 14) suggests that the dissolution/lithification cycles leading to stabilization of these structures occurs entirely under continuous hypersaline conditions. Accordingly, the influence of major storm events, which would result in correlative C and O isotopic signatures, indicative of kinetic fractionation (Craig et al., 1963), seems unlikely to contribute to the lithification and stabilization of these structures. By contrast, the correlation between some trace metal concentration and $\delta^{13}C$ in the thrombolites reflects the interplay between biotic and abiotic processes. The heavier carbon isotopic composition is indicative of a progressive depletion of available organic matter as it is used as an energy source by chemoheterotrophic microorganisms within the structure. Depletion of labile organic matter locally led to higher pore water alkalinities and CO_3^{2-} activities which promoted the incorporation of Mg^{2+} and other cations having similar enthalpies of hydration into secondary isotopically-heavier carbonate phases (e.g., Nissenbaum et al., 1972; Wright, 1999).

6. A modern analog to ancient gypsum-dominated microbialites

The microbialites from Laguna Pirata are comparable with massive, gypsified stromatolitic structures from the mid-Miocene (Badenian) of the eastern Ukraine and Poland (Peryt, 1996; Peryt et al., 2004; Babel, 2007), and also with less spectacular centimeter-scale examples of stromatolitic build-ups associated with gypsum that are known in the Messinian of western Cyprus, Sicily and Crete; Paleogene of Bresse, France, and Neogene of Egypt (Pierre and Rouchy, 1988; Rouchy and Monty, 2000, and references therein). Because gypsum is rarely found forming domal thrombolitic structures today (Rouchy and Monty, 2000), the thrombolites from Laguna Pirata offer a rare opportunity to examine the microbial role in the formation and preservation of gypsum-dominated microbialites.

These microbialites also allow us to extrapolate the biogeochemical processes that may have led to the development of microbialites in Late Archean to Proterozoic evaporitic environments, where comparable pseudomorphic fabrics occurred (El Tabakh et al., 1999; Pope and Grotzinger, 2003; Hardie, 2004; Sumner, 2004; Schröder et al., 2008), but for which the primary mineralogy remains largely unknown. For instance, the primary mineralogy of some meter-scale domes exhibiting pseudomorphic fabrics could have been either gypsum or aragonite, the latter being proposed based on petrographic and trace element data (Sumner and Grotzinger, 2000; Sumner, 2004; but see Hardie, 2003, 2004 for a discussion). In this regard, the relatively high concentrations of Sr in pseudomorphic aragonite after gypsum in the thrombolites from Laguna Pirata (Table 3) suggests that using strontium concentrations to delineate primary mineralogy may only apply if the source of Sr in the pseudomorphic calcite was seawater. If metastable aragonite forms after gypsum then the Sr of calcite replacing the aragonite may completely mask that of the older sulfate precursor.

Thus, the use of strontium may not be clear-cut in resolving the issue of primary mineralogy of pseudomorphic fabrics in ancient microbialites.

7. Conclusions

1. In Laguna Pirata the production of EPS by photoautotrophic microbial mats and its subsequent degradation by an associated heterotrophic community promotes the accretion of gypsum-dominated thrombolites that grow along the shallow rim of the lagoon.
2. Within the thrombolites, spatially and temporally complex dissolution/precipitation reactions, mediated by the metabolic activity of anoxygenic bacterial communities, lead to pseudomorphic replacement of gypsum by aragonite, accompanied by the occurrence of extracellular elemental sulfur accumulations and intragranular Mg-enriched microcrystalline cementation.
3. As a result of the ongoing microbially catalyzed early diagenetic reactions, metastable aragonite is prone to become successively replaced by more stable carbonate phases. These also lead to most extracellular S^0 deposits within the fossil porous thrombolitic fabric to be cycled by sulfide dependent communities interacting with BSR.
4. Among the most influential parameters potentially affecting the progressive calcification of gypsum microbialites is the amount of organic compounds trapped during accretion because its degradation resulted in localized increased zones of alkalinity in which Mg-enriched calcites may subsequently precipitate.
5. The trace metal signatures in the secondary cements are correlative with degradation states of organic matter as inferred by mineralogical assemblages: aragonite + elemental sulfur vs. aragonite + Mg-calcite, and their elemental distribution.
6. By contrast, the abundance of gypsum and the deficiency of carbonate in the unlithified organic sediment formed in the deepest part of the lagoon suggest that conditions in this zone prevented the formation of complex photosynthetic microbial mats and thus, thrombolite development. As a consequence, the dissolved sulfide produced in the bottom sediment is likely to be oxidized to form sulfate, which in turn, reacts with dissolved Ca^{2+} to form gypsum granules (or gypsooids).
7. The timing and processes of microbially-induced replacement and lithification of modern gypsum-rich microbialites, and their resulting biogeochemical signatures, are crucial in trying to ascertain biogeochemical signatures in ancient microbialites, particularly considering that the ancient counterparts have been subjected to billions of years of post-depositional modifications.

Acknowledgments

We thank Dr Karlis Muehlenbachs who provided us with valuable support for stable isotope data acquisition and Dee-Ann Rollings for her help with the SEM. The careful and insightful reviews of Dr R. Pamela Reid and Dr Brian Jones improved significantly the quality of this manuscript, in this regard their editorial effort, and that of anonymous reviewers are greatly acknowledged Dr Robert Riding and Dr Aubrey Zerkle provided helpful suggestions and corrections. Fieldwork was undertaken with the permission of the Instituto Nacional de Parques,Venezuela (INPARQUES) that granted access to the study site and allowed the collection of samples. Funding for this work was provided by the Natural Sciences and Engineering Research Council to Canada (NSERC) to K.O.K and M.K.G.

References

Aitken, J.D., 1967. Classification and environmental significance of crypt- algal limestones and dolomites, with illustrations from the Cambrian and Ordovician of southwestern Alberta. Journal of Sedimentary Petrology 37, 1163–1178.
Amend, T., 1992. Los habitantes del archipiélago en el pasado y el presente. In: Amend, T. (Ed.), Parque Nacional Archipiélago Los Roques: Parques Nacionales y Conservación Ambiental No. 3 (Caracas, Editorial Torino) 1–42 pp.
Amjad, Z., 1996. Scale inhibition in desalination applications: an overview. Corrosion, NACE 96–230.
Andres, M., Reid, R.P., 2006. Growth morphologies of modern marine stromatolites: a case study from Highborne Cay, Bahamas. Sedimentary Geology 185, 319–328.
Babel, M., 2004. Models for evaporite, selenite and gypsum microbialite deposition in ancient saline basins. Acta Geologica Polonica 54, 219–249.
Babel, M., 2007. Depositional environments of a salina-type evaporite basin recorded in the Badenian gypsum facies in the northern Carpathian Foredeep. Geological Society, London, Special Publication 285, 107–142.
Berner, R.A., 1975. The role of magnesium in the crystal growth of calcite and aragonite from seawater. Geochimica et Cosmochimica Acta 39, 489–604.
Braissant, O., Decho, A.W., Dupraz, C., Glunk, C., Przekop, K.M., Visscher, P.T., 2007. Exopolymeric substances of sulfate-reducing bacteria, interactions with calcium at alkaline pH and implication for formation of carbonate minerals. Geobiology 5, 401–411.
Braissant, O., Decho, A.W., Przekop, K.M., Gallagher, K.L., Glunk, C., Dupraz, C., Visscher, P.T., 2009. Characteristics and turnover of exopolymeric substances in a hypersaline microbial mat. FEMS Microbiology Ecology 67, 293–307.
Brand, U., 1994. Morphochemical and replacement diagenesis of carbonates. In: Wolf, K.H., Chilingarian, G.V. (Eds.), Diagenesis IV Developments Sedimentology 51. Elsevier, Amsterdam, pp. 217–282.
Buczynski, C., Chafetz, H.S., 1993. Habit of bacterially induced precipitates of calcium carbonate: examples from laboratory experiments and recent sediments. In: Rezak, R., Lavoie, D.L. (Eds.), Carbonate Microfacies. Springer-Verlag, New York, pp. 105–116.
Burne, R.V., Moore, L.S., 1987. Microbialites: organosedimentary deposits of benthic microbial communities. PALAIOS 2, 241–254.
Canfield, D.E., Thamdrup, B., Hansen, J.W., 1993. The anaerobic degradation of organic matter in Danish coastal sediments: iron reduction, manganese reduction, and sulfate reduction. Geochimica et Cosmochimica Acta 57, 3867–3883.
Cody, R.D., Cody, A.M., 1988. Gypsum nucleation and crystal morphology in analog saline terrestrial environments. Journal of Sedimentary Research 58, 247–255.
Cody, R.D., Cody, A.M., 1991. Crystal habit modifications of gypsum from epitaxial-like adsorption of stereospecific growth inhibitors. Journal of Crystal Growth 113, 508–519.
Craig, H., 1957. Isotopic standards for carbon and oxygen and correction factors for mass-spectro-metric analysis of carbon dioxide. Geochimica et Cosmochimica Acta 12, 133–149.
Craig, H., 1961. Standard for reporting concentrations of deuterium and oxygen-18 in natural waters. Science 133, 1833–1834.
Craig, H., Gordon, L.I., Horibe, Y., 1963. Isotopic exchange effects in the evaporation of sea water. Journal of Geophysical Research 68, 5079–5087.
Decho, A.W., 1990. Microbial exopolymer secretions in ocean environments: their role(s) in food webs and marine processes. Oceanography and Marine Biology: An Annual Review 28, 73–153.
Decho, A.W., 2010. Overview of biopolymer-induced mineralization: what goes on in biofilms? Ecological Engineering 36, 137–144.
Decho, A.W., Visscher, P.T., Reid, R.P., 2005. Production and cycling of natural microbial exopolymers (EPS) within a marine stromatolite. Palaeogeography, Palaeoclimatology, Palaeoecology 219, 71–86.
Des Marais, D.J., 2003. Biogeochemistry of hypersaline microbial mats illustrates the dynamics of modern microbial ecosystems and the early evolution of the biosphere. The Biological Bulletin 204, 160–167.
Doğanp, Ö., Akyolp, E., Önerp, M., 2004. Polyelectrolytes inhibition effect on crystallization of gypsum. Crystal Research and Technology 39, 1108–1114.
Dravis, J., Yurewicz, D., 1985. Enhanced carbonate petrography using fluorescence microscopy. Journal of Sedimentary Petrology 55, 795–804.
Dupraz, C., Visscher, P.T., 2005. Microbial lithification in marine stromatolites and hypersaline mats. Trends in Microbiology 13, 429–438. Available at: http://linkinghub.elsevier.com/retrieve/pii/S0966842X05001976 [Accessed March 25, 2011].
El Tabakh, M., Grey, K., Pirajno, F., Schreiber, B.C., 1999. Pseudomorphs after evaporitic minerals interbedded with 2.2 Ga stromatolites of the Yerrida basin, Western Australia: origin and significance. Geology 27, 871–874.
Fazio, S.A., Uhlinger, D.J., Parker, J.H., White, D.C., 1982. Estimations of uronic acids as quantitative measures of extracellular and cell wall polysaccharide polymers from environmental samples. Applied and Environmental Microbiology 43, 1151–1159.
Feldmann, M., McKenzie, J.A., 1998. Stromatolite–thrombolite associations in a modern environment, Lee Stocking Island, Bahamas. PALAIOS 13, 201–212.
Fernández-Díaz, L., Pina, C.M., Astilleros, J.M., Sánchez-Pastor, N., 2009. The carbonation of gypsum: pathways and pseudomorph formation. American Mineralogist 94, 1223–1234.
Flemming, H.C., Wingender, J., 2010. The biofilm matrix. Nature Reviews Microbiology 8, 623–633.
Folk, R.L., 1993. S.E.M. imaging of bacteria and nannobacteria in carbonate sediments and rocks. Journal of Sedimentary Petrology 63, 990–999.
Friedman, I., O'Neil, J.R., 1977. Compilation of stable isotope fractionation factors of geochemical interest, In: Fleisher, M. (Ed.), Data of Geochemistry, 6th ed. : USGS Prof. Paper 440.
Gerdes, G., Krumbein, W.E., Noffke, N., 2000. Evaporite microbial sediments. In: Riding, R.E., Awramik, S.M. (Eds.), Microbial sediments. Springer-Verlag, Berlin, pp. 196–208.
Grotzinger, J.P., Knoll, A.H., 1999. Stromatolites in Precambrian carbonates, evolutionary mileposts or environmental dipsticks? Annual Review of Earth and Planetary Sciences 27, 313–358.
Hardie, L.A., 2003. Secular variations in Precambrian seawater chemistry and the timing of Precambrian aragonite seas and calcite seas. Geology 31, 785–788.

Hardie, L.A., 2004. Secular variations in Precambrian seawater chemistry and the timing of Precambrian aragonite seas and calcite seas. Reply to Dr. Dawn Sumner Comment. Geology 32, e1–e2.
Hunter, K.S., Wang, Y.F., Van Cappellen, P., 1998. Kinetic modeling of microbially driven redox chemistry of subsurface environments: coupling transport, microbial metabolism and geochemistry. Journal of Hydrology 209, 53–80.
Jarosewich, E., 2002. Smithsonian microbeam standards. Journal of Research of the National Institute of Standards and Technology 107, 681–685.
Jørgensen, B.B., Revsbech, N.P., Cohen, Y., 1983. Photosynthesis and structure of benthic microbial mats: microelectrode and SEM studies of four cyanobacterial communities. Limnology and Oceanography 28, 1075–1093.
Kah, L.C., Lyons, T.W., Chesley, J.T., 2001. Geochemistry of a 1.2 Ga carbonate–evaporite succession, northern Baffin and Bylot Islands: implications for Mesoproterozoic marine evolution. Precambrian Research 111, 203–234.
Kalkowsky, E., 1908. Oolith und Stromatolith im norddeutschen Buntsandstein. Deutschen Geologische Gesellschaft 60, 68–125.
Kamber, B.S., Bolhar, R., Webb, G.E., 2004. Geochemistry of late Archaean stromatolites from Zimbabwe: evidence for microbial life in restricted epicontinental seas. Precambrian Research 132, 379–399. Available at: http://linkinghub.elsevier.com/retrieve/pii/S0301926804000816 [Accessed February 9, 2011].
Kaufman, E.N., Little, M.H., Selvaraj, P.T., 1996. Recycling of FGD gypsum to calcium carbonate and elemental sulfur using; mixed sulfate-reducing bacteria with sewage digest as a carbon source. Journal of Chemical Technology and Biotechnology 66, 365–374.
Kennard, J.M., James, N.P., 1986. Thrombolites and stromatolites: two distinct types of microbial structures. PALAIOS 1, 492–503.
Kobluk, D.R., Crawford, D.R., 1990. A modern hypersaline organic mud- and gypsum-dominated basin and associated microbialites. PALAIOS 5, 134–148.
Kobluk, D.R., Risk, M.J., 1977. Calcification of exposed filaments of endolithic algae, micrite envelope formation and sediment production. Journal of Sedimentary Petrology 47, 517–528.
Last, W.M., Schweyen, T.H., 1983. Sedimentology and geochemistry of saline lakes of the Great Plains. Hydrobiologia 105, 245–263.
Lee, D., Carpenter, S.J., 2001. Isotopic disequilibrium in marine calcareous algae. Chemical Geology 172, 307–329.
Liss, S.N., Droppo, I.G., Flannigan, D.T., Leppard, G.G., 1996. Floc architecture in wastewater and natural riverine systems. Environmental Science and Technology 30, 680–686.
McCrea, J.M., 1950. On the isotopic chemistry of carbonates and a paleotemperature scale. Journal of Chemistry and Physics 18, 849–857.
Nissenbaum, A., Baedecker, M., Kaplan, I., 1972. Organic geochemistry of Dead Sea sediments. Geochimica et Cosmochimica Acta 36, 709–727.
Ortega-Morales, B.O., Santiago-García, J.L., Chan-Bacab, M.J., Moppert, X., Miranda-Tello, E., Fardeau, M.L., Carrero, J.C., Bartole-Perez, P., Valandez-Gonzalez, A., Guezennec, J., 2007. Characterization of extracellular polymers synthesized by tropical intertidal biofilm bacteria. Journal of Applied Microbiology 102, 254–264.
Parkhurst, D.L., Appelo, C.A.J., 1999. User's guide to PHREEQC (version 2)-A computer program for speciation, batch-reaction, one-dimensional transport, and inverse geochemical calculations. U.S. Geological Survey Water-Resources Investigations Report 99-4259, 312 p.
Peckman, J., Paul, J., Thiel, V., 1999. Bacterially mediated formation of diagenetic aragonite and native sulphur in Zechstein carbonates (Upper Permian, Central Germany). Sedimentary Geology 126, 205–222.
Perry, T., Klepac-Ceraj, V., Zhang, X.V., McNamara, C.J., Polz, M.F., Martin, S.T., Berke, N., Mitchell, R., 2005. Binding of harvested bacterial exopolymers to the surface of calcite. Environmental Science and Technology 39, 8770–8775.
Peryt, T.M., 1996. Sedimentology of Badenian (Middle Miocene) gypsum in eastern Galicia, Podolia and Bukovina (West Ukraine). Sedimentology 43, 571–588.
Peryt, T.M., Peryt, D., Jasionowski, M., Poberezhskyy, A.V., Durakiewicz, T., 2004. Post-evaporitic restricted deposition in the Middle Miocene Chokrakian-Karaganian of east Crimea (Ukraine). Sedimentary Geology 170, 21–36.
Pierre, C., Rouchy, J.M., 1988. Carbonate replacements after sulphate evaporates in the Middle Miocene of Egypt. Journal of Sedimentary Petrology 58, 446–456.
Planavsky, N., Ginsburg, R.N., 2009. Taphonomy of modern marine Bahamian microbialites. PALAIOS 24, 5–17.
Pope, M.C., Grotzinger, J.P., 2003. Paleoproterozoic Stark Formation, Athapuscow Basin, Northwest Canada: record of cratonic-scale salinity crisis. Journal of Sedimentary Research 73, 280–295.
Pope, M.C., Grotzinger, J.P., Schreiber, B.C., 2000. Evaporitic Subtidal Stromatolites Produced by in situ Precipitation: Textures, Facies Associations, and Temporal Significance. Journal of Sedimentary Research 70, 1139–1151.
Reid, R.P., Macintyre, I.G., 2000. Microboring versus recrystallization: further insight into the micritization process. Journal of Sedimentary Research 70, 24–28.
Reid, R.P., Macintyre, I., James, N., 1990. Internal precipitation of microcrystalline carbonate: a fundamental problem for sedimentologists. Sedimentary Geology 68, 163–170.
Revsbech, N.P., Jørgensen, B.B., Blackhurn, T.H., Cohen, Y., 1983. Microelectrode studies of photosynthesis and O_2, H_2S and pH profiles of microbial mat. Limnology and Oceanography 28, 1062–1074.
Riding, R., 2000. Microbial carbonates: the geological record of calcified bacterial-algal mats and biofilms. Sedimentology 47, 179–214.
Riding, R., 2008. Abiogenic, microbial and hybrid authigenic carbonate crusts: components of Precambrian stromatolites. Geologia Croatica 61, 73–103.
Riding, R., 2011. Microbialites, stromatolites , and thrombolites. In: Reitner, V., Thiel, J. (Eds.), Encyclopaedia of Geobiology. : (Encyclopaedia of Earth Sciences Series). Springer, Heidelberg, pp. 635–654.
Rouchy, J.M., Monty, C., 2000. Gypsum microbial stromatolites: neogene and modern examples. In: Riding, R.E., Awramik, S.M. (Eds.), Microbial sediments. Springer, Berlin, pp. 209–216.
Schröder, S., Bekker, A., Beukes, N.J., Strauss, H., van Niekerk, H.S., 2008. Rise in seawater sulphate concentration associated with the Paleoproterozoic positive carbon isotope excursion: evidence from sulphate evaporites in the 2.2–2.1 Gyr shallow-marine Lucknow Formation, South Africa. Terra Nova 20, 108–117.
Shapiro, R.S., 2000. A comment on the systematic confusion of thrombolites. PALAIOS 15, 166–169.
Slaughter, M., Hill, R.J., 1991. The influence of organic matter in organogenic dolomitization. Journal of Sedimentary Research 61, 296–303.
Sonnenfeld, P., 1984. Brines and Evaporite. Academic Press Inc.. 613 pp.
Sonnenfeld, P., Hudec, P.P., Turek, A., Boon, J.A., 1977. Base-metal concentration in a density stratified evaporite pan. In: Fischer, J.H. (Ed.), Reefs and evaporites—concepts and depositional models: AAPG Studies in Geology, pp. 181–187.
Spurr, A.R., 1969. A low-viscosity epoxy resin embedding medium for electron microscopy. Journal of Ultrastructure Research 26, 31–43.
Stal, L.J., 2000. Cyanobacterial mats and stromatolites. In: Whitton, B.A., Potts, M. (Eds.), The Ecology of Cyanobacteria: Their Diversity in Time and Space. Kluwer Academic Publishers, Dordrecht, pp. 61–120.
Stefess, G.C., Torremans, R.A.M., De Schrijver, R., Robertson, L.A., Kuenen, J.G., 1996. Quantitative measurement of sulphur formation by steady-state and transient-state continuous cultures of autotrophic *Thiobacillus* species. Applied Microbiology and Biotechnology 45, 169–175.
Sumner, D.Y., 2004. Secular variations in Precambrian seawater chemistry and the timing of Precambrian aragonite seas and calcite seas-Comment. Geology 32, e1–e2.
Sumner, D.Y., Grotzinger, J.P., 2000. Late Archean aragonite precipitation: petrography, facies associations, and environmental significance. In: Grotzinger, J.P., James, N.P. (Eds.), Carbonate Sedimentation and Diagenesis in the Evolving Precambrian World. SEPM Special Publication 67, pp. 123–1443. Available at: http://sp.sepmonline.org/content/sepspecpub/sepspcab/1/SEC8.body.pdf [Accessed March 25, 2011].
Thompson, J.B., Ferris, F.G., 1990. Cyanobacterial precipitation of gypsum, calcite, and magnesite from natural alkaline lake water. Geology 18, 995–998.
Tribovillard, N., Algeo, T., Lyons, T., Riboulleau, A., 2006. Trace metals as paleoredox and paleoproductivity proxies: an update. Chemical Geology 232, 12–32.
Turner, E.C., James, N.P., Narbonne, G.M., 2000. Taphonomic control on microstructure in early neoproterozoic reefal stromatolites and thrombolites. PALAIOS 15, 87–111.
van den Ende, F.P., van Gemerden, H., 1993. Sulfide oxidation under oxygen limitation by a Thiobacillus thioparus isolated from a marine microbial mat. FEMS Microbiology Ecology 13, 69–77.
van Gemerden, H., 1993. Microbial mats: a joint venture. Marine Geology 113, 3–25.
Visscher, P.T., Stolz, J.F., 2005. Microbial mats as bioreactors, populations, processes, and products. Palaeogeography, Palaeoclimatology, Palaeoecology 219, 87–100.
Visscher, P.T., Reid, R.P., Bebout, B.M., Hoeft, S.E., Macintyre, I.G., Thompson, J.A., 1998. Formation of lithified micritic laminae in modern marine stromatolites (Bahamas): the role of sulfur cycling. American Mineralogist 83, 1482–1493.
Vogel, M.B., Des Marais, D.J., Turk, K.A., Parentau, M.N., Jahnke, L.L., Kubo, M.D.Y., 2009. The role of biofilms in the sedimentology of actively forming gypsum deposits at Guerrero Negro, Mexico. Astrobiology 9, 875–893.
Vogel, M., Des Marais, D., Parenteau, M.N., et al., 2010. Biological influences on modern sulfates: textures and composition of gypsum deposits from Guerrero Negro, Baja California Sur, Mexico. Sedimentary Geology 223, 265–280.
Wright, D.T., 1999. The role of sulphate-reducing bacteria and cyanobacteria in dolomite formation in distal ephemeral lakes of the Coorong region, South Australia. Sedimentary Geology 126, 147–157.
Wright, D.T., Wacey, D., 2005. Precipitation of Dolomite Using Sulphate-Reducing Bacteria from the Coorong Region, South Australia: Significance and Implications.